Simulation of peri-receptive field inhibition in primary visual cortex

2023 Master's Thesis Yokohama City University Graduate School

Department of Materials and System Sciences, Graduate School of Life Nanosystem Sciences

Shunryo Yoshida

Table of Contents

Executive Summary 1
1 Introduction 5
1.1 Background 5
1.2 Objective 5
2 Fundamentals of Computational Neuroscience 6
1.1 Neurophysiology 6
1.2 Typical Neural Circuit Model 6
3 previous research 8
3.1 Primary visual field model 8
3.2 Peri-receptive field suppression 8
4 Development of a primary visual field model 11
5 Simulation of peri-receptive field inhibition 15
5.1 Reproduction of peri-receptive field inhibition by a model of primary visual cortex 15
5.2 Analysis of peri-receptive field inhibition outside of layer 2/3 and synchronous oscillation under peri-receptive field inhibition 19
5.3 Comparative analysis under unstimulated and peri-receptive field suppression onset 23
6 CONCLUSIONS. 28
7 Acknowledgements 30
8 Research Publications 31
9 References 33

Simulation of peri-receptive field inhibition in primary visual cortex

Full name: Shunryo Yoshida

Primary Supervisor: Professor Micheletto Ruggiero

Sub-supervisors: Professor Masashi Tachikawa, Professor Kazuo Yoshimoto, Associate Professor Shinji Nonose

Simulation of peri-receptive field inhibition in primary visual cortex

Simulation of Surround Suppression in Primary Visual Cortex

Department of Materials and Systems Science Instructor Shunryo Yoshida Michelette Ruggiero

Primary visual cortex: brain region responsible for early visual processing located in the occipital region of the neocortex

Peripapillary inhibition: a phenomenon in which an increase in visual stimulus size is accompanied by a response of decreased activity of excitatory neurons within the stimulus range. An important function in perception that has been pointed out to be related to detection of object curvature. LIF model: A model in which neurons are constructed as simple electrical circuits

Spike: electrical signal indicating a sudden increase in voltage in a neuron

Research Background and Objectives

The brain is responsible for diverse information processing related to sensation and movement in living organisms. Therefore, investigation of the information processing mechanisms of the brain will lead to an understanding of the perception and behavior of living organisms, including humans. Moreover, clarifying the information processing mechanisms that support such biological activities will lead to the elucidation of the computational mechanisms of neurological diseases and the development of medical and engineering fields such as artificial intelligence and brain-learned computers.

In order to investigate the phenomenon called peri-receptive field suppression from a computational approach, we will develop a new model of the primary visual cortex that is faithful to the cell density and binding probability of the actual mouse brain. Furthermore, the developed model will be used to reproduce peri-receptive field inhibition and to analyze responses and neural oscillation states in regions not investigated experimentally. Specifically, we will develop a model of the primary visual cortex of the resting state mouse, reproduce peri-receptive inhibition under stimulus presentation in column 2/3 of the primary visual cortex, and analyze the effects in other layers not observed in experiments and the neural oscillation state during the occurrence of peri-receptive inhibition. Through this analysis, we aim to gain a more detailed understanding of peri-receptive inhibition.

[Claire] How do you do it?

The mouse primary visual cortex model in this study is based on data such as cell density, connectivity probability, synaptic connectivity strength, and axonal delay in [1], and the LIF model is used to construct a network of primary visual cortex models.

The LIF model has parameters such as firing time constants for four types of neurons: excitatory Pyr, inhibitory SOM, PV, and Htr3A. The primary visual cortex model has a columnar structure, consisting of layers 1, 2/3, 4, 5, and 6, with layer 1 containing Htr3A and layers 2/3 to 6 containing Pyr, SOM, PV, and Htr3A (Figure 1 left) Each combination of each neuronal population is coupled according to coupling parameters (coupling probability and coupling weight). The network was created by NEST simulator, a neural circuit simulation software. The cellular arrangement of the network was set up in a lattice shape in order to have uniform

connections (Figure 1, right)

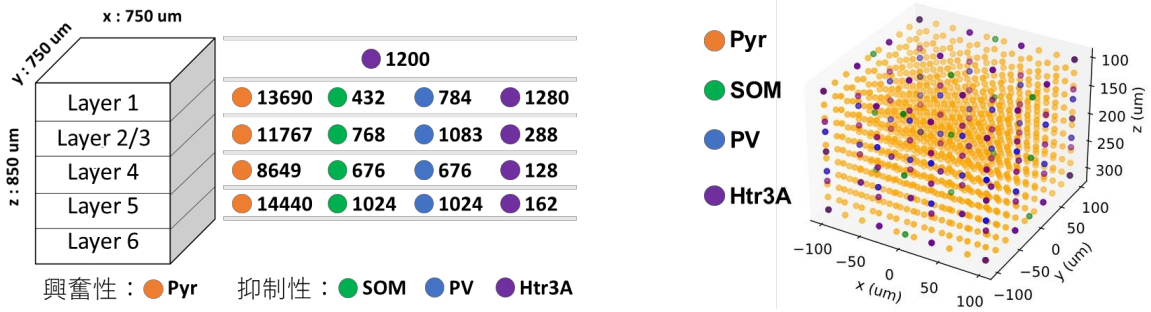

Figure 1. Model size and number of neurons (left) and partial regions of the created model (right)

Results and Discussion

In order to reproduce the unstimulated state during waking, the firing rates of neurons in the waking state of mice are used as a reference, and spike trains following a Poisson process are input to Pyr, SOM, PV, and Htr3A. The activity firing rates of the neural network are adjusted based on the results of physiological experiments [2].

The created model was simulated for 2500 ms with a time step of 0.1 ms, and the average firing rate change for the entire column was analyzed, excluding the first 500 ms. Figure 2 Left: Raster showing the firing timing of each neuron

The plots are. The colors correspond to those of the neuron types shown in the left panel of Figure 1. The spike counts were determined as the change in spike counts every 5 ms from the left side of Figure 2, and then the changes were analyzed by Fourier transform to identify the peak of synchronous gamma oscillation at 35-40 Hz. Since synchronous oscillation is a characteristic neural activity, w e defined this as the state during waking and unstimulated condition in this study.

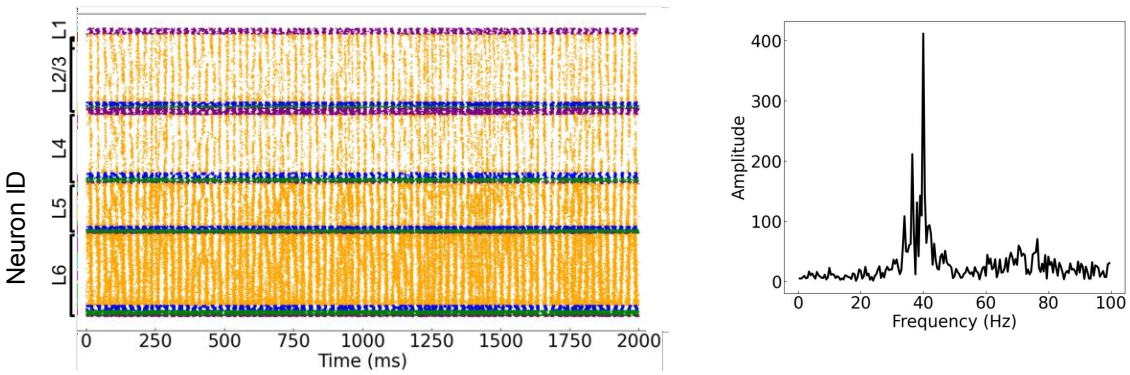

Figure 2. Raster plot (left) and frequency spectrum (right) showing ignition timing

In the replication of peri-receptive field inhibition, current stimuli of different ranges and intensities were applied to layer 2/3 of the model as shown on the left side of Figure 3. Simulations were performed for all combinations of range and intensity, and the results are summarized on the right side of Figure 3, where the minimum and maximum average firing rates of Pyr, SOM, PV, and VIP within the range of layer 2/3 stimulation were normalized to 0 and 1, respectively. The figure shows that at a current intensity of 40 pA, the activity of Pyr and PV decreases in response to the increased activity of SOM, well replicating the results of physiological experiments [2]. However, as the current intensity increases away from 40 pA, they also depart from the experimental results. Especially when the stimulus range is 720 um, the experimental results are significantly different from the experimental results.

The response is often out of line with the results, but this is thought to be due to the fact that the model is 750 um square, which is close to the model boundary, and thus exhibits unstable behavior. In addition, simulations showed that Htr3A responds similarly to Pyr and PV, which had not been experimentally confirmed. In addition, we confirmed that inhibitory cells respond differently in deeper layers, which have not been investigated in physiological experiments.

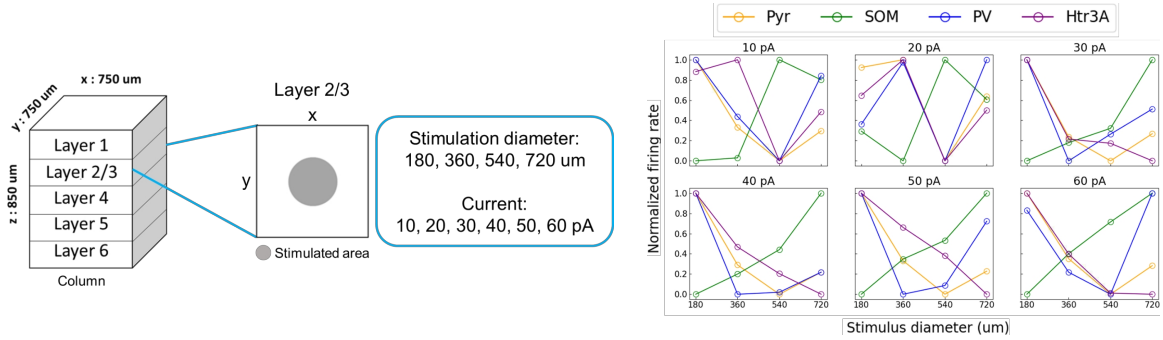

Figure 3. Stimulus conditions and schematic of peri-receptive field inhibition (left) and response to each stimulus condition (right)

Furthermore, a frequency analysis similar to Figure 2 was performed based on the raster plots under peri-receptive field suppression and the temporal changes in the number of spikes, but no differences were found. Therefore, we developed the frequency analysis and analyzed the temporal frequency change by spectrogram. A spectrogram is a method to visualize the temporal change of frequency as an image in which the horizontal axis represents time, the vertical axis represents frequency, and the color represents intensity. The spectrogram created by the Fourier transform using a time window is shown in Figure 4 (left). Here, we used the intensity in units of decibels calculated as $\log_{10} A$ when the original signal intensity is A. The left side of this figure corresponds to unstimulated and the right side to peri-receptive field inhibition. To clarify the difference, the signal intensities under unstimulated and peri-receptive field suppression are A_1 and A_2 , respectively, and the output intensity, $\log_{10} A\ /A_{21}$, is shown in Figure 4, right. After conversion to logarithm, it is the same as calculating the intensity difference in Figure 4 left. The way we see it is that, with reference to the unstimulated condition, a red color indicates a strong synchronous oscillation under peri-receptive field inhibition in that frequency band, and a blue color indicates a weak one. The results show that the peaks under peri-receptive inhibition are relatively stronger at various frequencies up to around 1 second. On the other hand, after that, the peaks around 40 Hz and 80 Hz gradually become stronger, and the peak under non-stimulation is stronger over a wider range. Thus, it is clear, therefore, that in the present simulation, the peaks in the specific frequency bands as described above are particularly stronger under peri-receptive field suppression.

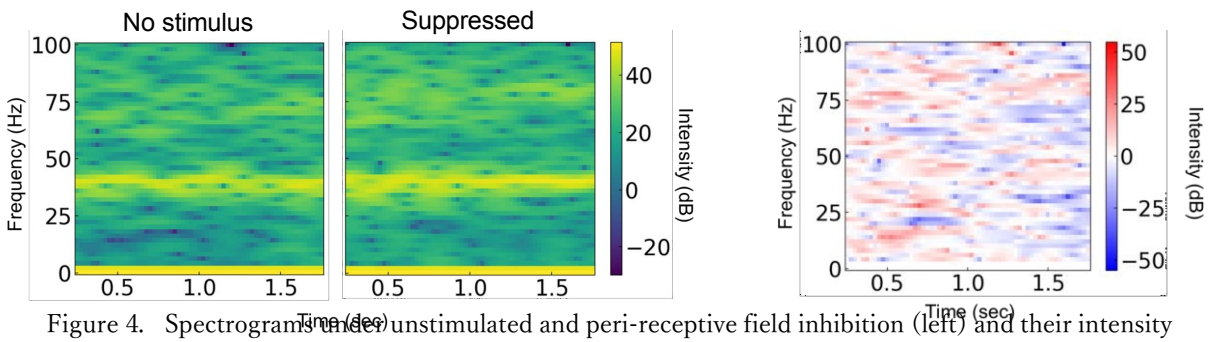

Figure 4. Spectrograms under unstimulated and peri-receptive field inhibition (left) and their intensity differences (right)

Finally, the temporal relationship between firing rates was analyzed by visualizing them on a two-dimensional plane. The temporal variation of firing rates can be obtained from the change in the number of spikes every 5 ms in Figure 2 and the number of cells in the column. Figure 5(a) visualizes the firing rate (FR) at one time and the next time on the horizontal and vertical axes, respectively. The results show that when the point cloud is under suppression between 500 and 1500 ms, it is characterized by a blank space in the interior of the point cloud. To investigate this feature quantitatively, we used persistent homology, a method of topological data analysis, to examine the hole structure present in the point cloud over the entire time for each state (Fig.
5(b)). The characteristic hole structure found in Figure 5(b) was obtained by inverse analysis, as shown in Figure 5(c), revealing that there is indeed a blank structure inside the point cloud under the peri-receptive field suppression.

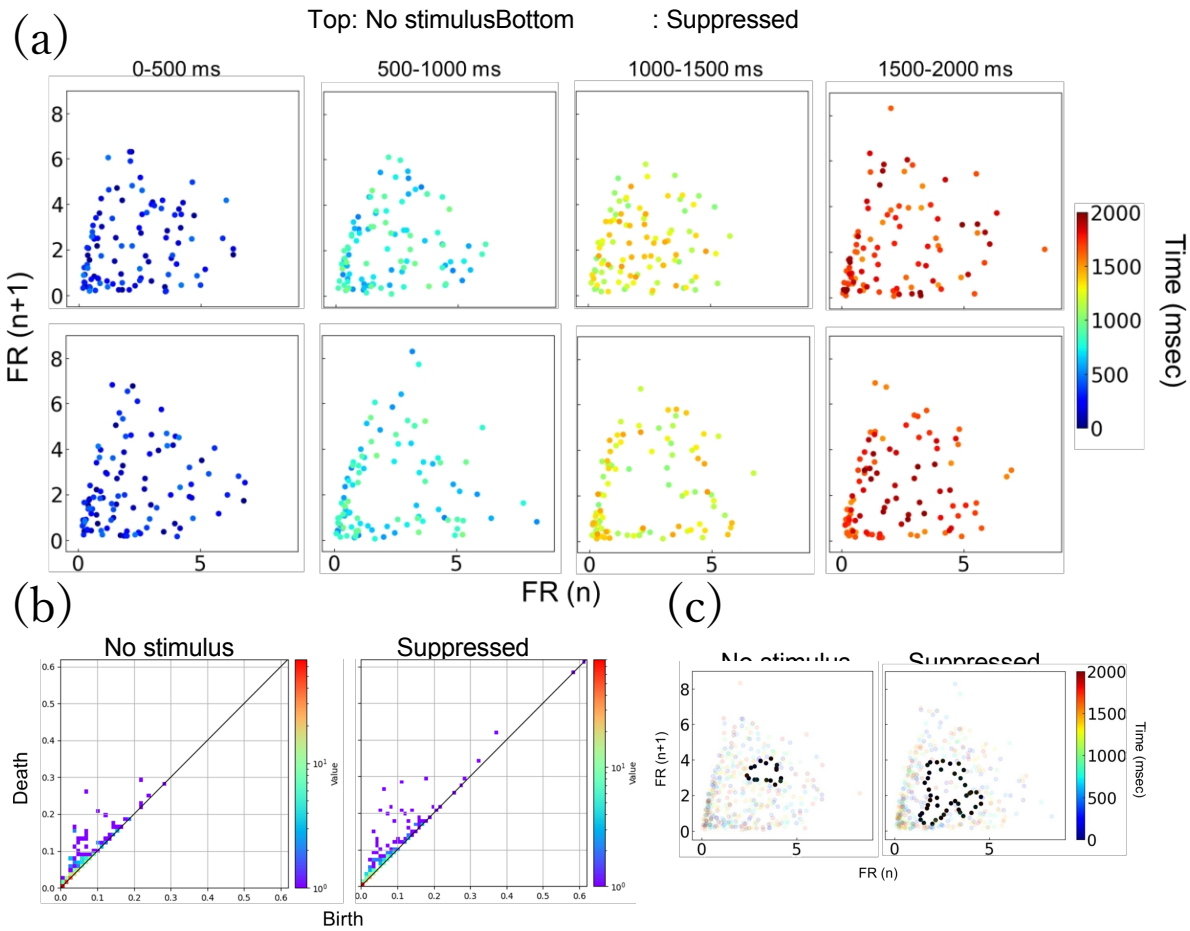

Figure 5. (a) Temporal relationship between firing rates,(b) Persistent diagram analysis of the point cloud in (a), (c) Group of points (black dots) corresponding to the characteristic structure obtained by inverse analysis from the persistent diagram.

[References

[1] Billeh, Y.N. et al. *Neuron*, 106, 1-16. (2020).

[2] Adesnik, H. et al. *Nature*. 490(7419), 226-231.(2012).

1 introduction

1.1 background

The brain is responsible for diverse information processing related to sensation and movement in living organisms. Therefore, investigation of the information processing mechanisms of the brain will lead to an understanding of the perception and behavior of living organisms, including humans. In addition, clarifying the information processing mechanisms that support such biological activities will lead to the elucidation of the computational mechanisms of neurological diseases and the development of medical and engineering fields such as artificial intelligence and brain-learned computers.

In the field of neuroscience, recent breakthroughs in measurement technology have provided many clues about the brain's information processing from physiological findings. On the other hand, another approach is to develop theoretical and computational models of the brain and to understand brain information processing by studying its behavior. These approaches support the development of neuroscience on both fronts: theory to explain experiments and experiments to find phenomena predicted by theory.

1.2 Objective.

In order to investigate the phenomenon called peri-receptive field suppression from a computational approach, we will develop a new model of the primary visual cortex that is faithful to the cell density and binding probability of the a c t u a l mouse brain. Furthermore, the developed model will be used to reproduce peri-receptive field inhibition and to investigate its effects and neural oscillatory state in regions that have not been experimentally investigated. Specifically, we will develop a model of primary visual cortex in awake and unstimulated mice, reproduce peri-receptive inhibition under stimulus presentation in column 2/3 of primary visual cortex, and analyze the effects and neuronal oscillation state during peri-receptive inhibition in other layers that have not been observed in experiments. Through these analyses, we aim to gain a more detailed understanding of the mechanism of peri-receptive inhibition.

2 Fundamentals of Computational Neuroscience

In the following, we will introduce some of the neurophysiological terminology and representative neuronal models used in computational neuroscience that will be required in this study.

1.1 neurophysiology

Although differences exist among species, the brains of organisms have basically similar functions and structures. In this section, we will mainly discuss brain structures related to mammals.

The brain is composed of three major regions: cerebrum, cerebellum, and brainstem. The cerebrum is primarily responsible for sensory processing, the cerebellum for motor coordination, and the brainstem for basic life support [1-4].

In particular, in the neocortex, the part of the cerebrum treated in this study, there is a hierarchical structure with distinctive structures at each scale. The first hierarchies to appear are those that designate rough locations, such as the frontal and occipital lobes. Next are the scales specialized for each sensory information processing, which are called the foveas. In particular, the primary visual cortex, the area responsible for early visual information processing, is located in the occipital lobe. Furthermore, within a region, regions that respond to specific stimuli are grouped together and called columns. Columns are six-layered (the six-layer structure is not hierarchical, but a common feature of the entire neocortex), and within each layer, many neurons connect with each other and exchange electrical signals called spikes. The structure of a neuron consists of dendrites that receive input from other neurons, cell bodies that integrate stimuli, and axons that provide output to other neurons. Neurons are broadly classified into excitatory cells, which activate brain activity, and inhibitory cells, which deactivate brain activity, depending on the type of stimulus transmission. This difference is determined by the type of synaptic connections, which are the connections between neurons.

1.2 Typical Neural Circuit Model

Neural circuit modeling is a method to computationally and theoretically investigate neural activity by considering neurons and their populations in sensory organs and the brain as physical models, such as electrical circuits, and then formulating differential equations to calculate them [5-7].

Historically, Hodgkin and Huxley investigated the propagation of action potentials in squid giant axons in 1952 and obtained it as a four-variable nonlinear differential equation [8]. This model was called the HH model, but because it was a nonlinear differential equation in four variables, its response was difficult to understand intuitively.

In this context, FitzHugh and Nagumo considered the HH model as a kind of Van der Pol oscillator and obtained simplified neuronal behavior as a bivariate nonlinear differential equation [9,10]. This transformation into equations of few variables allowed the dynamics of neurons to be studied as a dynamical system using phase diagrams and other methods.

On the other hand, the Leaky Integrated and Fire model (LIF model) exists as a model that qualitatively reproduces the behavior of neurons, rather than biophysically quantitative and precise equations like the HH model. It was first developed by Lapicque in 1907 [11], and has been used in a number of studies, such as model refinement and efficiency improvement.

Research has been undertaken for a long time (Figure 1) This model is often used in large-scale simulations because of its advantage of computational simplicity due to its simple differential equations [7].

Furthermore, in a similar modeling vein to the LIF model, Izhikevich in 2003 developed a bivariate differential equation (with fewer variables than the HH model) that is known to reproduce neuronal behavior well [12].

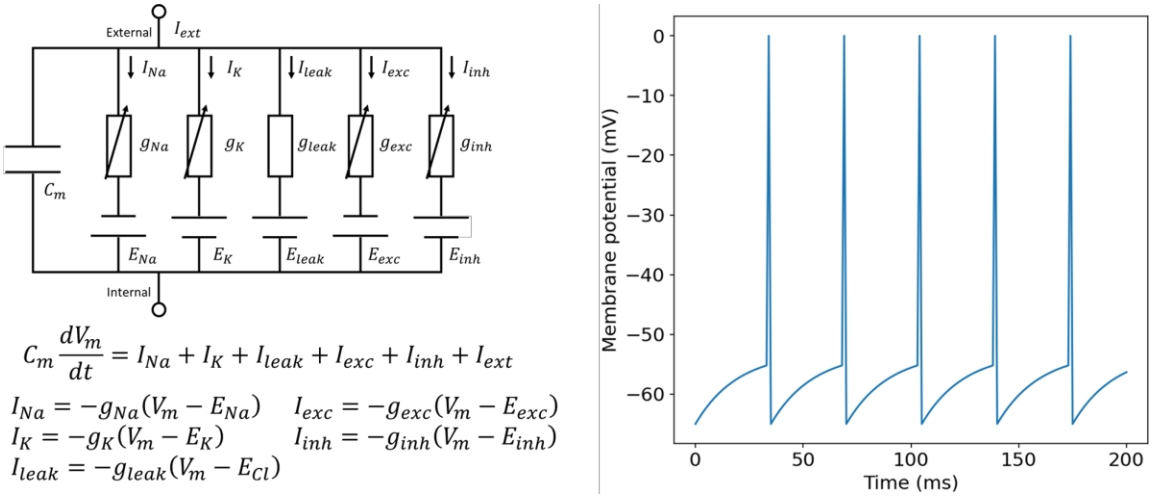

Figure 1. Representation of the LIF model in terms of electrical circuit and differential equations (left) and response (right)

3 previous work

In this chapter, we will discuss previous studies that are directly related to our research topic. The previous studies can be divided into two broad categories: experimental evidence on peri-receptive field suppression and studies on models of primary visual cortex based on actual cell densities.

3.1 primary visual cortex model

Because the primary visual cortex is responsible for early visual processing, it has been the subject of much research in neurophysiology. Early work by Hubel and Wiesel, who found neurons in the primary visual cortex of cats that responded selectively to line segments in specific directions [13], led to the investigation of the relationship between visual input and the primary visual cortex. In this context, physical and computational methods using neuronal models were introduced to gain a deeper understanding of the relationship between specific visual inputs and the neurons that respond selectively to them, allowing us to infer the processing taking place in the brain [14,15]. One of the early challenges in these fields was that simulating neuronal models and their networks required the numerical solution of a number of differential equations proportional to the size of the network, and only simple models could be handled due to computational limitations.

In recent years, however, large-scale simulations have become possible with the development of computers. For example, in [16], a large-scale simulation of the primary somatosensory cortex in rats was conducted using a neuronal model called the multicompartment model. In this vein, [17] performed a large-scale simulation of a primary visual cortex model in both the LIF model and the multi-compartment model based on actual mouse cell density and other data. However, this primary visual cortex model was adjusted to the average firing rate under specific visual stimulus presentation and did not reproduce the condition under non-stimulus conditions during waking. Therefore, it is necessary to construct a network based on the waking state under non-stimulus conditions in order to compare neural activity between the waking state under non-stimulus conditions and the state under some visual stimulus presentation.

3.2 periaqueductal inhibition

In the brains of mammals such as humans, cats, and mice, the retina and brain regions that respond to different types of stimuli are called classical receptive fields [1]. However, there is a response that cannot be interpreted by such classical receptive fields alone, a phenomenon called ambient modulation [18]. This is a phenomenon in which the response is modulated by differences in contextual information such as the size and number of visual stimuli, even when the types of visual stimuli being viewed are the same. Among these, the phenomenon of inhibitory responses due to ambient modulation is called receptive field ambient suppression. Such non-intuitive responses are pointed out to be related to perceptual functions such as curvature detection, motion, and speed of objects captured by the eye [18-20], and require basic understanding. As a specific example, in the visual cortex, an increase in visual stimulus size causes a decrease in the response of pyramidal cells (Pyr), which are excitatory cells inside the stimulus. However, there are cases in which the opposite is true for contour integration, where the response is facilitatory [20]. In addition, information-theoretic perspectives

from the Efficient Coding Hypothesis [21] and Sparse Coding [22].

Although many experimental facts exist, there is no unified view on what mechanism is responsible for the occurrence [18]. For example, several patterns have been proposed for the brain networks that cause ambient modulation: coupling with the retina and LGN in primary visual cortex [23,24], horizontal coupling within primary visual cortex [25], and coupling with higher-order areas such as secondary visual cortex [26]. The fact that there are experimental facts for all patterns suggests that they are complex, but the main elements, etc., are currently unknown [18].

Several models have been proposed that can explain such ambient modulation phenomena. Among those widely applicable to neural computation in general are the Normalization model [27], the Inhibition-stabilized networks model [28], and the Stabilized supralinear networks model [29]. These are characterized as explanatory models for explaining phenomena in that they can explain a wide range of neural activity but are phenomenologically structured and are not constrained to physiological data [30]. On the other hand, there are also computational models that reflect more physiological data [18,30]. Many of these are based on some assumption and simulations are performed by taking out a portion of the column structure of interest, and the entire column structure and neuron counts are not faithful to the physiological data.

In a previous study, which is the subject of this replication, it was shown in experiments on layer 2/3 of the mouse primary visual cortex that an increase in visual stimulus size increases the activity of somatostatin-expressing inhibitory neurons (SOM) and suppresses the excitatory Pyr, resulting in perireceptive field inhibition [31]. The mechanism was explained as an increase in stimulus range producing an increase in active Pyr in the periphery, which in turn increases the activity of SOM within the stimulus range and decreases the activity of Pyr within the stimulus range. However, these detailed responses have only been found in limited locations, such as layer 2/3, as described above, and how they respond in other locations and to different intensity stimuli has not been investigated. In addition, 5-hydroxytryptamine receptor 3A-expressing inhibitory neurons (Htr3A) have not been the subject of any experiments, although parvalbumin-expressing inhibitory neurons (PVs) have been simultaneously examined.

Trg / Src	i1Htr3a	E2/3	i2/3 Pvalb	i2/3 Sst	i2/3 Htr3a	E4	i4 Pvalb	i4 Sst	i4 Htr3a	E5	i5 Pvalb	i5 Ssst	i5 Htr3a	E6	i6 Pvalb	i6 Sst	i6 Htr3a
i1Htr3a	0.656	0.356	0.093	0.068	0.464	0.148				0.148	0	0		0.148			
E2/3	0	0.16	0.395	0.182	0.105	0.016	0.083	0.083	0.083	0.083	0.081	0.102		0			
i2/3Pva	0.024	0.411	0.451	0.03	0.22	0.05	0.05	0.05	0.05	0.07	0.073						
i2/3Sst	0.279	0.424	0.857	0.082	0.77	0.05	0.05	0.05	0.05	0.021		0					
i2/3Htr	0	0.087	0.02	0.625	0.028	0.05	0.05	0.05	0.05	0							
E4		0.14	0.1	0.1	0.1	0.243	0.43	0.571	0.571	0.104	0.101	0.128	0.05	0.032			
i4Pvalb		0.25	0.05	0.05	0.05	0.437	0.451	0.03	0.22	0.088	0.091	0.03	0.03				
i4Sst	0.241	0.25	0.05	0.05	0.05	0.351	0.857	0.082	0.77	0.026	0.03	0	0.03				
i4Htr3a		0.25	0.05	0.05	0.05	0.351	0.02	0.625	0.028	0	0.03	0.03	0.03				
E5	0.017	0.021	0.05	0.05	0.05	0.007	0.05	0.05	0.05	0.116	0.083	0.063	0.105	0.047	0.03	0.03	0.03
i5Pvalb	0	0	0.102			0	0.034	0.03	0.03	0.455	0.361	0.03	0.22	0.03	0.01	0.01	0.01
i5Sst	0.203	0.169		0.017		0.056	0.03	0.006	0.03	0.317	0.857	0.04	0.77	0.03	0.01	0.01	0.01
i5Htr3a						0.03	0.03	0.03	0.03	0.125	0.02	0.625	0.02	0.03	0.01	0.01	0.01
E6		0				0				0.012	0.01	0.01	0.01	0.026	0.145	0.1	0.1
i6Pvalb		0.1				0.1				0.1	0.03	0.03	0.03	0.1	0.08	0.1	0.08
i6Sst										0.03	0.03	0.03	0.03	0.1	0.05	0.05	0.05
i6Htr3a										0.03	0.03	0.03	0.03	0.1	0.05	0.05	0.03

Trg / Src	i1Htr3a	E2/3	i2/3 Pvalb	i2/3 Sst	i2/3 Htr3a	E4	i4 Pvalb	i4 Sst	i4 Htr3a	E5	i5 Pvalb	i5 Ssst	i5 Htr3a	E6	i6 Pvalb	i6 Sst	i6 Htr3a
i1Htr3a	1.73	0.53	0.48	0.57	0.78	0.42				0.42	0	0		0.42			
E2/3	0	0.36	1.49	0.86	1.31	0.34	1.39	0.69	0.91	0.74	1.32	0.53		0			
i2/3Pva	0.37	0.48	0.68	0.42	0.41	0.56	0.68	0.42	0.41	0.2	0.79						
i2/3Sst	0.47	0.31	0.5	0.15	0.52	0.3	0.5	0.15	0.52	0.22		0					
i2/3Htr	0	0.28	0.18	0.32	0.37	0.29	0.18	0.32	0.37	0							
E4		0.78	1.39	0.69	0.91	0.83	1.29	0.51	0.51	0.63	1.25	0.52	0.91	0.96			
i4Pvalb		0.56	0.68	0.42	0.41	0.64	0.68	0.42	0.41	0.73	0.94	0.42	0.41				
i4Sst	0.39	0.3	0.5	0.15	0.52	0.29	0.5	0.15	0.52	0.28	0.45	0.28	0.52				
i4Htr3a		0.29	0.18	0.32	0.37	0.29	0.18	0.32	0.37	0	0.18	0.33	0.37				
E5	0.76	0.47	1.25	0.52	0.91	0.38	1.25	0.52	0.91	0.75	1.2	0.52	1.31	0.4	2.5	0.52	1.31
i5Pvalb	0	0	0.51			0	0.94	0.42	0.41	0.81	1.19	0.41	0.41	0.81	1.19	0.41	0.41
i5Sst	0.31	0.25		0.39		0.28	0.45	0.28	0.52	0.27	0.4	0.4	0.52	0.27	0.4	0.4	0.52
i5Htr3a						0.29	0.18	0.33	0.37	0.28	0.18	0.33	0.37	0.28	0.18	0.33	0.37
E6		0				0				0.23	2.5	0.52	1.31	0.94	3.8	0.52	1.31
i6Pvalb		0.81				0.81				0.81	1.19	0.41	0.41	0.81	1.19	0.41	0.41
i6Sst										0.27	0.4	0.4	0.52	0.27	0.4	0.4	0.52
i6Htr3a										0.28	0.18	0.33	0.37	0.28	0.18	0.33	0.37

Figure 2. Joint probabilities (left) and joint weights (right) for [17]

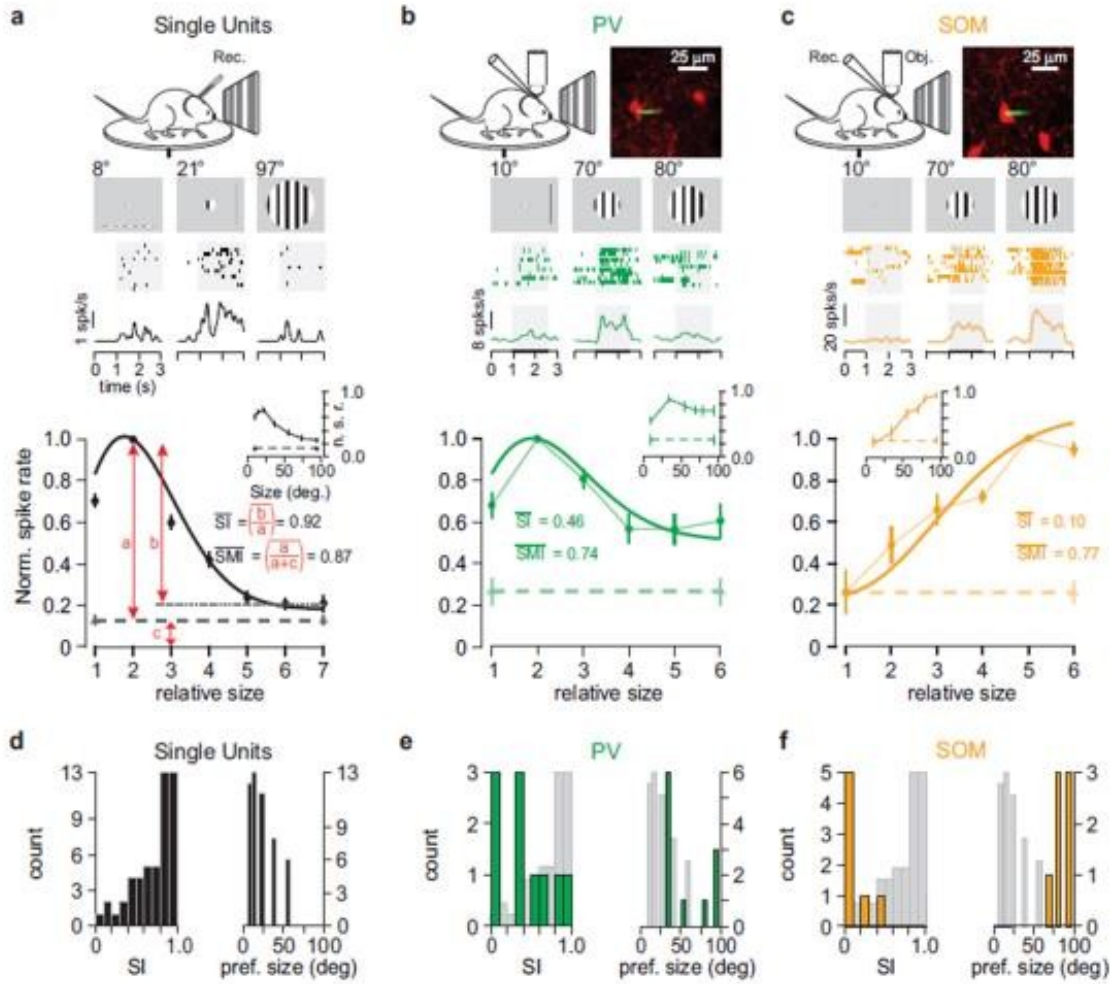

Figure 3 Response of Pyr, PV, and SOM during the occurrence of peri-receptive field suppression [31].

4 Development of a primary visual field model

The mouse primary visual cortex model in this study is based on data such as cell density, connectivity probability, synaptic connectivity strength, and axonal delay in [17], and the LIF model is used to construct the primary visual cortex model.

In the previous study, the LIF model parameters were determined for each cell type, which were further subdivided than Pyr,SOM,PV,andHtr3A. The LIF model was developed by setting parameters such as time constants for firing for the four neuron types (Pyr, SOM,PV,andHtr3A) in the LIF model. The main difference is that PV is faster than SOM and PV is slower than SOM. The main difference is that PVs are called fast spiking neurons and fire more frequently, while Pyr and SOMs are called regular spiking neurons and fire less frequently than PVs [32]. which is the largest proportion of both types of Htr3A [33,34]. The primary visual cortex model has a column structure similar to that of [17] and consists of layers 1, 2/3, 4, 5, and 6, with layer 1 containing Htr3A and layers 2/3 through 6 containing Pyr, SOM, PV, and Htr3A (Figure 4) Each combination of neuronal populations is coupled according to coupling parameters (Figure 5) Among the coupling parameters, the coupling weights are given by the postsynaptic currents in [17], so the conductances were determined so that the postsynaptic currents agree with the data in the paper within 1% error by simulating and numerically exploring the conductance values in each combination by gradually changing them from 0 to The coupling probability depends on the horizontal distance. The coupling probability was set so that the coupling probability decreases in a Gaussian fashion depending on the horizontal distance. In addition, synaptic plasticity was not introduced in the present model.

The network thus configured is used in NEST, a neural circuit simulation software. It was created using version 3.3 of simulator [35] (Figure 6) Here, the cellular arrangement of the network was set to a lattice shape in order to have uniform connectivity.

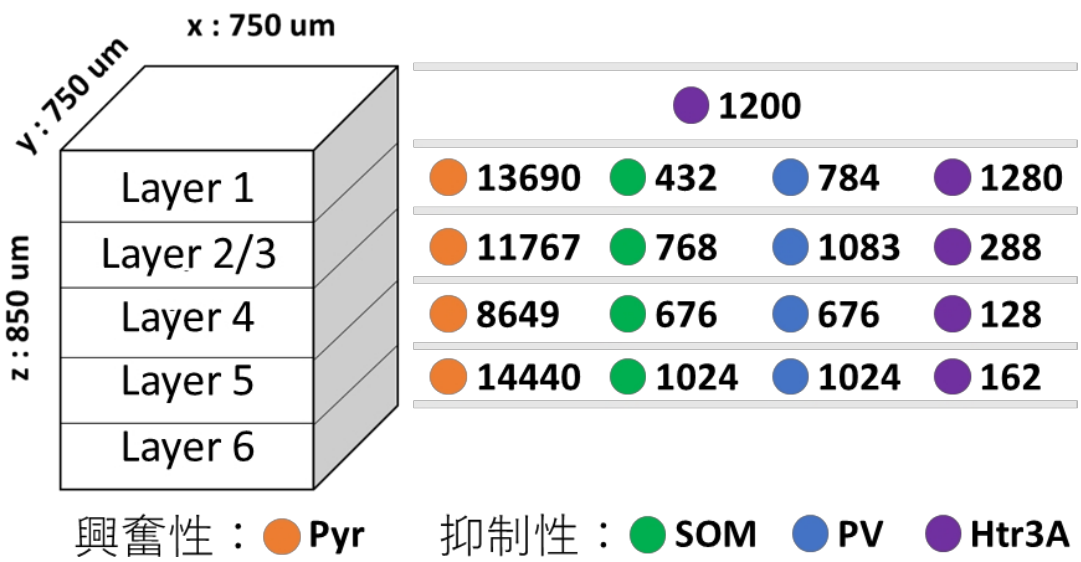

Figure 4. Column Structure and Number of Cells in Each Layer

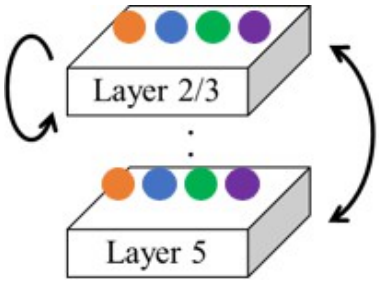

Target / Source	L1 Htr3A	L23 Pyr	· · ·
L1 Htr3A	0.656	0.356	· · ·
L23 Pyr	0	0.16	· · ·
· · ·	· · ·	· · ·	· · ·

Figure 5. Schematic diagram of intra- and interlaminar coupling (left) and cell population coupling parameter settings (right)

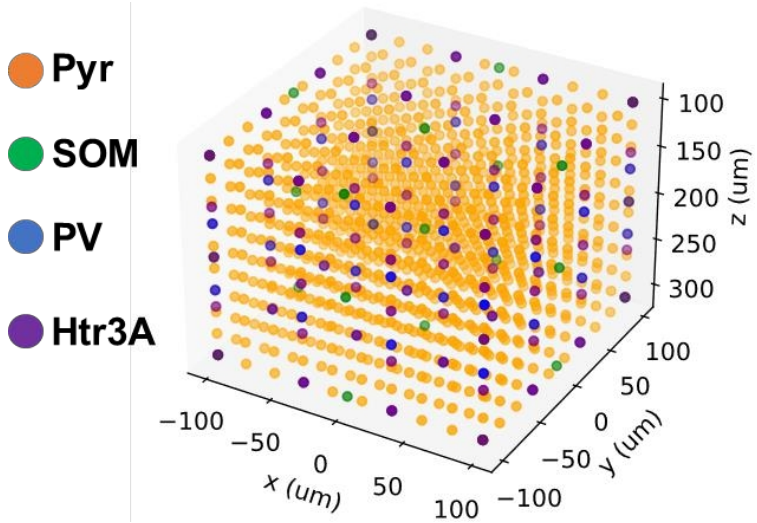

Figure 6. Model of primary visual cortex with neurons arranged in a grid pattern

In order to reproduce the unstimulated state during waking, we used [31, 36,37] as the firing rate of neurons in the waking state of mice as a reference and adjusted the activity state of the neural network by inputting spike trains following a Poisson process to Pyr, SOM, PV, and Htr3A. For layer 2/3, which is the main target in this study, the firing rates were adjusted to be within 60% error range of the experimental values (Table 1) For the other layers, the Pyr values were also within the experimental error range. On the other hand, due to the lack of information on the average firing rate of each inhibitory neuron type in layers 2/3 and below, the firing rates were adjusted to have a similar trend to the large and small average firing rates according to cell type in layer 2/3 and the average firing rate of Pyr in each layer. The model created as described above was simulated using the fourth-order Runge-Kutta method with a time step set to 0.1 ms. The simulation time was 2500 ms, except for the first 500 ms to remove transient responses, and the average firing rate change over the entire column was analyzed. First, a raster plot showing the firing timing of each neuron is created in Figure 7. To see, the horizontal axis is time and the vertical axis is an index designating which neuron is which, arranged from the top starting with the first layer. The dotted area indicates the neuron with the index specified on the vertical axis.

The timing of cell firing is shown, and the colors correspond to the colors for each cell type shown in Figure 6. Results in Figure 7

To determine the change in the number of spikes from the spike number, the total change in the number of spikes per 5 ms was obtained (Figure 8) Frequency analysis of the spike count change by Fourier transform revealed a peak of γ oscillation, which is a synchronous oscillation of about 35-40 Hz (Figure 9)

These synchronous oscillations are characteristic activities of neuronal populations in the actual brain [38], and it has been pointed out that γ oscillations, in particular, facilitate information processing among synchronous oscillations [39]. For example, it has been shown that γ oscillations define the timing of the transmission of sensory information to Pyr [40] and that noise is reduced in the transmission of information from Pyr to PV [41] [42].

Thus, γ-synchronous oscillations are an effective neural activity in information processing, and we will use this as the waking and unstimulated state in this study.

Table 1. Comparison of experimental and model firing rates for each neuron type in layers 2/3

	発火率（実験）	発火率（モデル）
Pyr	0.47 ± 0.11 Hz	0.36 Hz
PV	9 ± 2 Hz	10.27 Hz
SOM	7 ± 2 Hz	3.10 Hz
Htr3A	3.9 ± 0.6 Hz	3.65 Hz

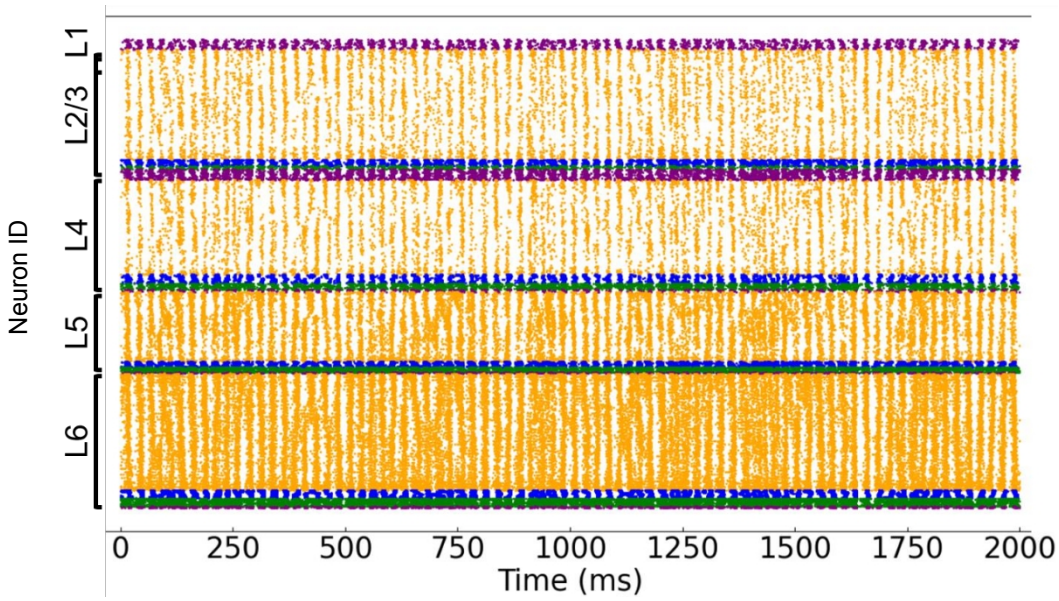

Figure 7. Raster plot after firing rate adjustment

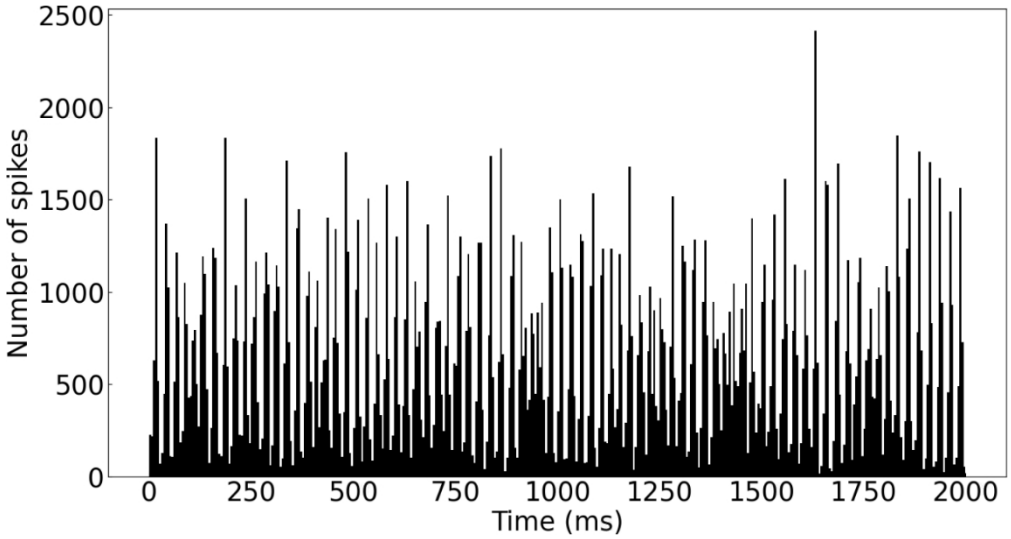

Figure 85 Change in total spikes per ms

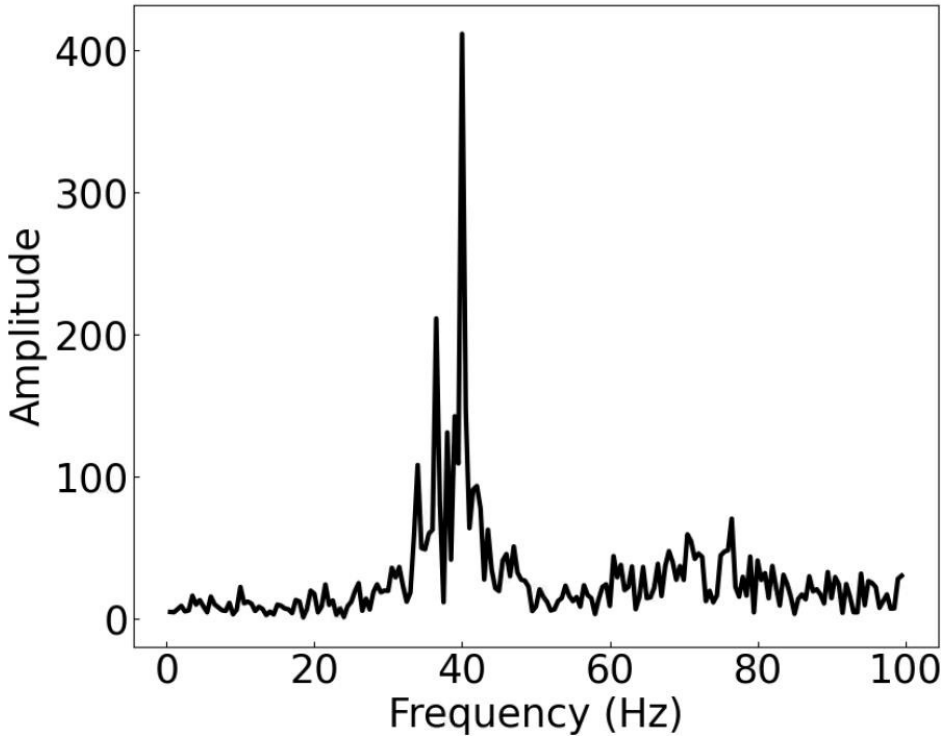

Figure 9. Frequency analysis results of total spike count change

5 Simulation of peri-receptive field inhibition

5.1 Reproduction of peri-receptive field inhibition by primary visual cortex model

We aim to reproduce peri-receptive field inhibition by applying stimuli corresponding to physiological experiments to a resting state model of the primary visual cortex that we have constructed and tuned. In the experiment of [31], which is the subject of this study, experiments are conducted in mice that have been modified by optogenetics to cause depolarization by exposing neurons to laser light, resulting in neural spikes. In this study, what was stimulation by laser light in the actual experiment is given to the model as electric current stimulation to simulate the physiological experiment. In addition, we will investigate the response of the model in detail by varying not only the stimulus range as in the physiological experiments but also the intensity of the current stimulus corresponding to the intensity of the laser light.

The specific stimulation range this time was the 2nd/3rd layer, and as shown in Figure 10, the results of current stimulation of various intensities were analyzed in four different circular areas with diameters of 180 um, 360 um, 540 um, and 720 um, located at the center in the x-y plane. The current stimulation intensity was set at 10 pA, 20 pA, 30 pA, 40 pA, 50 pA, and 60 pA.

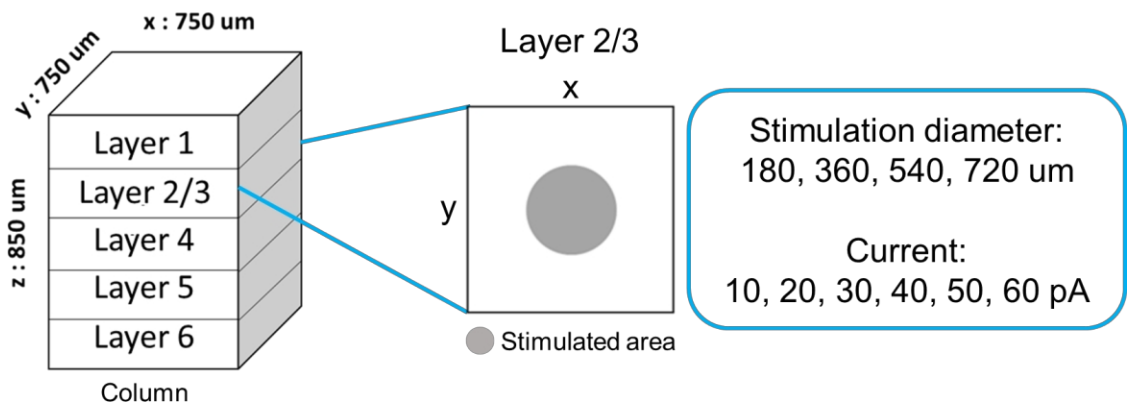

Figure 10. Schematic diagram of stimulus presentation to primary visual cortex model

Figure 11 summarizes the results of running the simulations for all combinations of stimulus range and intensity, normalizing the minimum value of the average firing rate of Pyr, SOM, PV, and VIP within the second/third layer stimulus range to 0 and the maximum value to 1. Figure 11 shows that at a current intensity of 40 pA, the Pyr and PV activity decreases in response to the increase in SOM activity, a result that well replicates the results of the physiological experiments. However, it can be seen that as the current intensity increases away from 40 pA, the results also diverge from the experimental results. In particular, when the stimulus range is 720 um, the response often deviates significantly from the experimental results, but this is thought to be due to the fact that the model range is 750 um square, which is close to the model boundary, and thus the response shows unstable behavior. The simulation results also show that Htr3A responds similarly to Pyr and PV, which had not been experimentally confirmed.

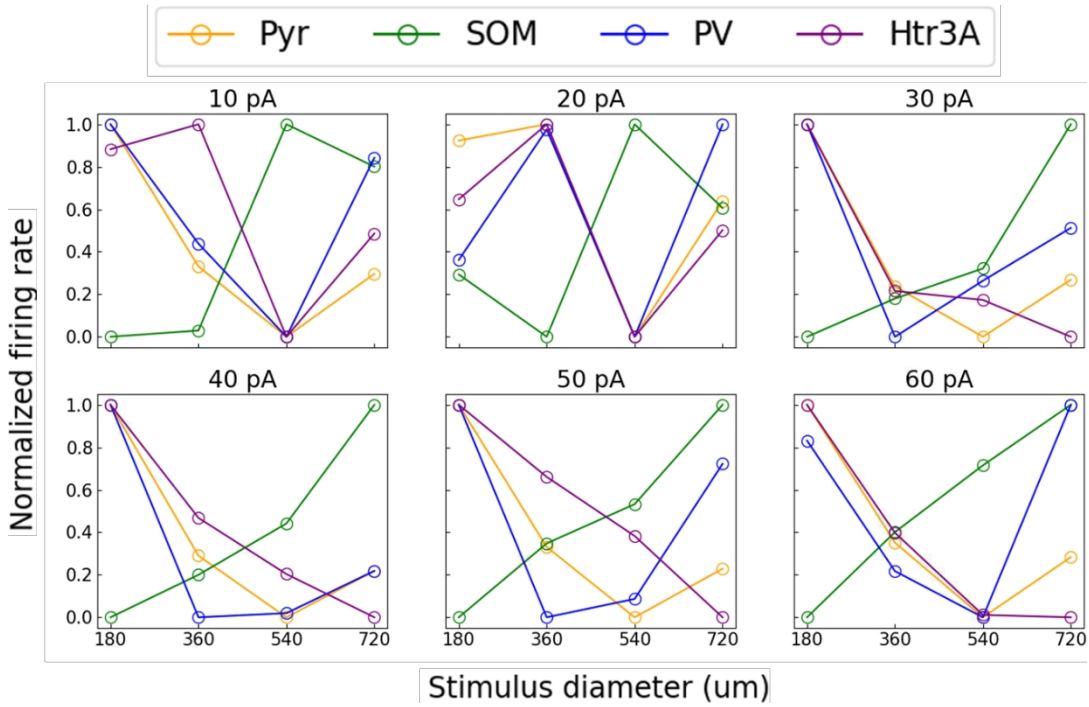

Figure 11. Simulation results of peri-receptive field suppression in layer 2/3

Suppression Index (SI) exists as a method to evaluate peri-receptive field inhibition by index values, in addition to judging it by the figure and firing rate. This method is calculated as the difference between the mean firing rate normalized by a different rule than Figure 11 and the mean firing rate under non-stimulus conditions. Specifically, the normalized firing rate is obtained by dividing all the average firing rates by the maximum value of the average firing rate for each stimulus intensity, and then the difference between 1 and the normalized firing rate under unstimulated conditions (A) is divided by the difference between 1 and the normalized firing rate in the maximum stimulus range (B) to obtain the SI (Figure 9) The SI for each neuron type is calculated in Figures 12 to 15.

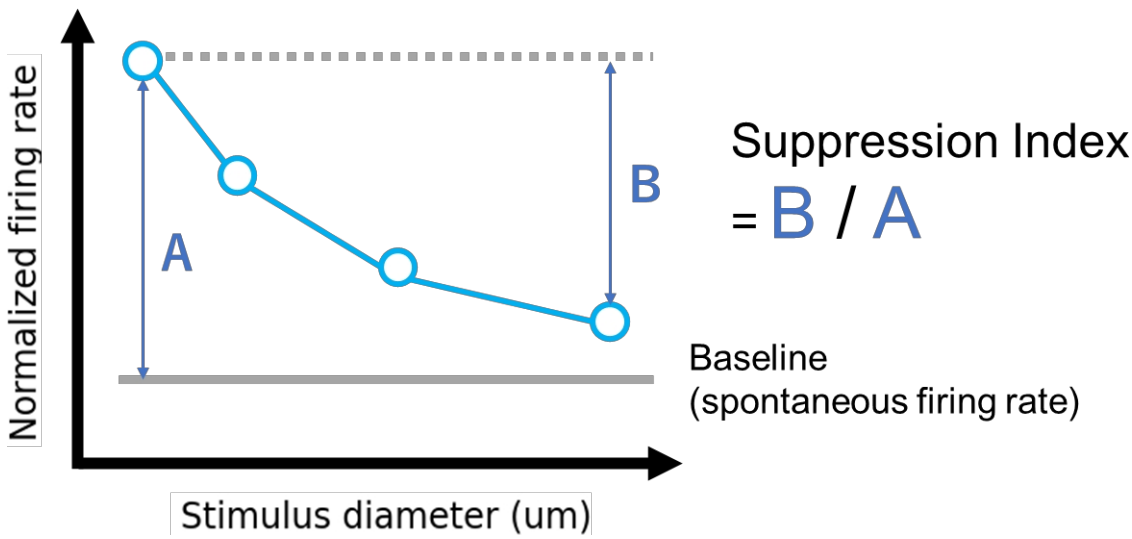

Figure 11: Suppression Index Calculation Method

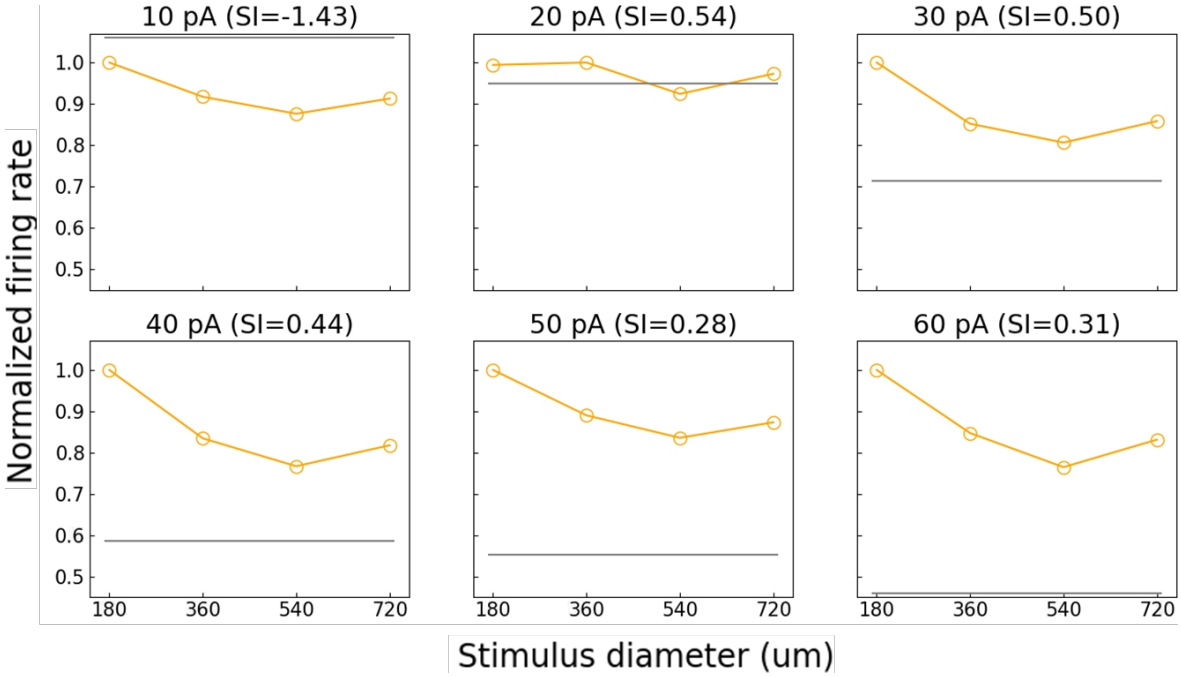

Figure 12Pyr's response including reference value and SI

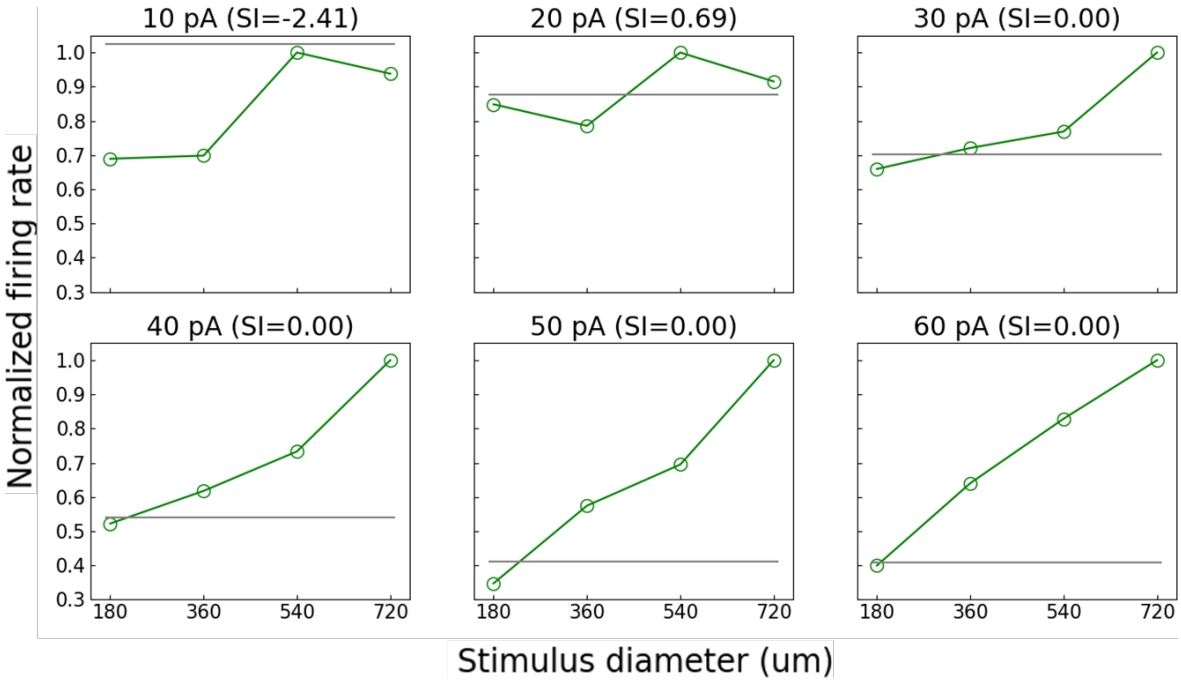

Figure 13 SOM response including reference value and SI

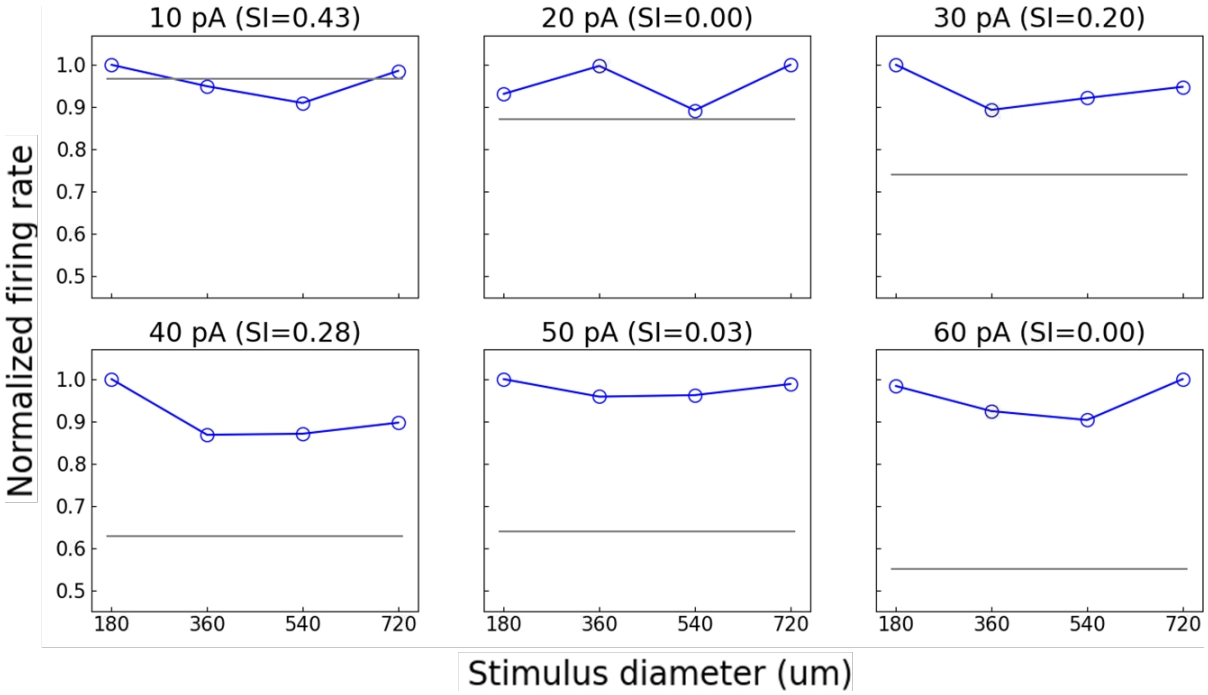

Figure 14PV response including reference value and SI

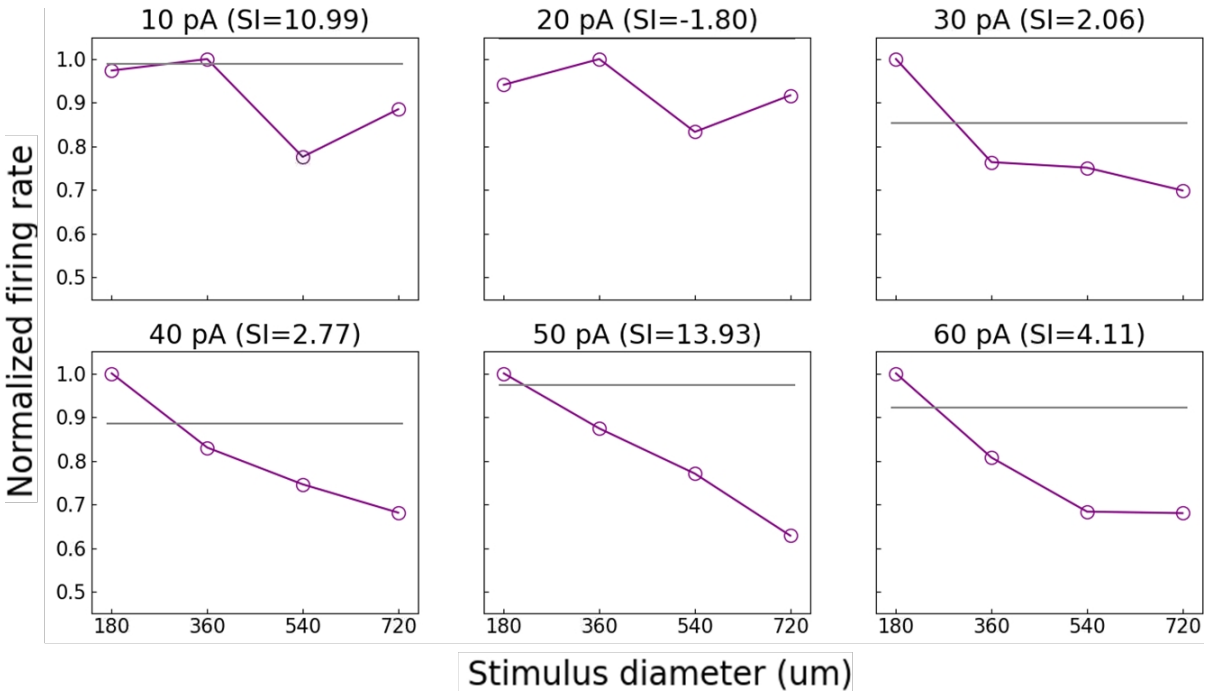

Figure 15Htr3A response including reference value and SI

The figure also shows that the effect of peri-receptive field inhibition is well reproduced at 40 pA stimulation. 30 pA for Pyr is indicatively more effective for inhibition, but this may be due to the fact that the results of the boundary condition are greatly influenced by the maximum stimulation range of 540 um, which is much closer to the actual results. However, the results of Htrs. However, for Htr3A, which was not observed in the experiment, the index values differ significantly from those of other neuronal cell types because the standard unstimulated firing rate is located between the maximum and minimum firing rates under stimulation. The SI may be insufficient to capture these Htr3A responses as well. By comparing the SI obtained in the above manner with the SI obtained from the experiment, it became clear that the SI had a similar trend to the value obtained from the simulation in this study, and the effect of peri-receptive field inhibition could be quantitatively verified by the index value.

Table 2Comparison of Suppression Index with experimental values

	Pyr	SOM	music video	VIP
Experimental values [31].	0.92	0.10	0.46	-
Simulated value (40 pA)	0.44	0.0 (0.0)	0.28	2.77

5.2 Analysis of peri-receptive field inhibition outside of layer 2/3 and synchronous oscillation under peri-receptive field inhibition

So far, we have analyzed the response of layer 2/3 only, but here we will analyze the response of deeper layers. Specifically, we examine the response of the deeper layers while simulating the peri-receptive field inhibition in the 2nd/3rd layer. The analysis method is the same as for the 2nd/3rd layer, with the minimum value of the average firing rate set to 0 and the maximum value set to 1, to investigate the effect of peri-receptive field suppression (Figs. 16-18) In this section, we mainly consider the responses to circular stimuli with diameters of 180 um, 360 um, and 540 um in order to exclude unstable behavior when stimuli are applied to the vicinity of the model boundary.

Figure 16 shows the response of layer 4, and it can be seen that the peri-receptive field inhibition of Pyr occurs in layer 4 as in layer 2/3. However, in layer 2/3, the peri-receptive inhibition of Pyr was caused by the SOM, whereas in layer 4, the inhibitory neurons dominant for the peri-receptive inhibition of Pyr were changed to PV and Htr3A. This reverses the role of inhibitory neuron types in layers 2/3. A possible factor in the present simulation is that the role reversal may be caused by inhibitory neurons interfering with each other due to differences in the density of each cell and interlaminar connections not only within layers. Next, looking at the response of layer 5 from Figure 17, it can be observed that the SOM is effective in peri-receptive field inhibition, although its detailed behavior differs from that of layer 2/3. However, in layer 2/3, all neurons are inhibited at the same time during 40 pA stimulation, which is the best replication of the experiment, and this phenomenon cannot be treated simply by the intralaminar relationship. Finally, layer 6 in Figure 18 shows that Htr3A behaves effectively as a peri-receptive field inhibitor. This is interesting in that a neuron type not observed in the experiment plays an effective role.

A common feature of the deep layers that distinguishes them from layers 2/3 is that the response of Pyr's peri-receptive field inhibition is more pronounced in the stimulus range.

The shift to the broad directional side of the In particular, in a related study, the receptive field circumference of layer 6

Since this shift in response to the right side was even confirmed as a result of the simulation of enclosure inhibition, we believe that the results are consistent with other computational models as well [30]. Thus, we have confirmed that not only the role of inhibitory neurons changes as the stimulus is transmitted through interlaminar connections, but also that such a shift occurs simultaneously.

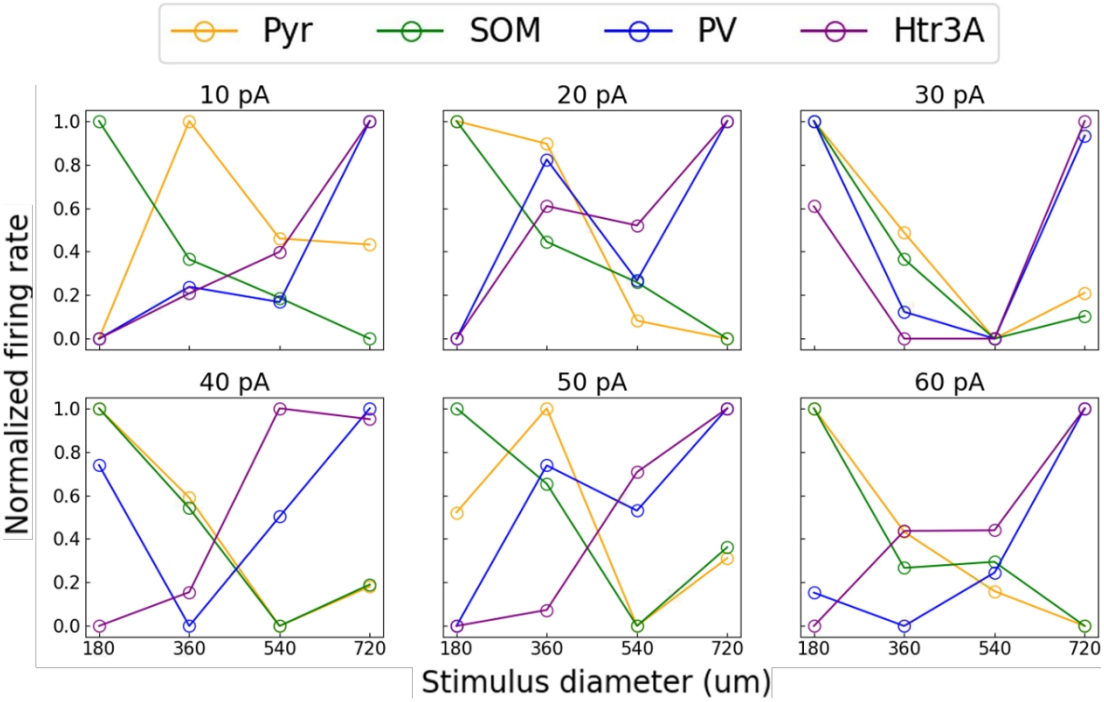

Figure 16. Layer 4 response during simulation of peri-receptive field inhibition

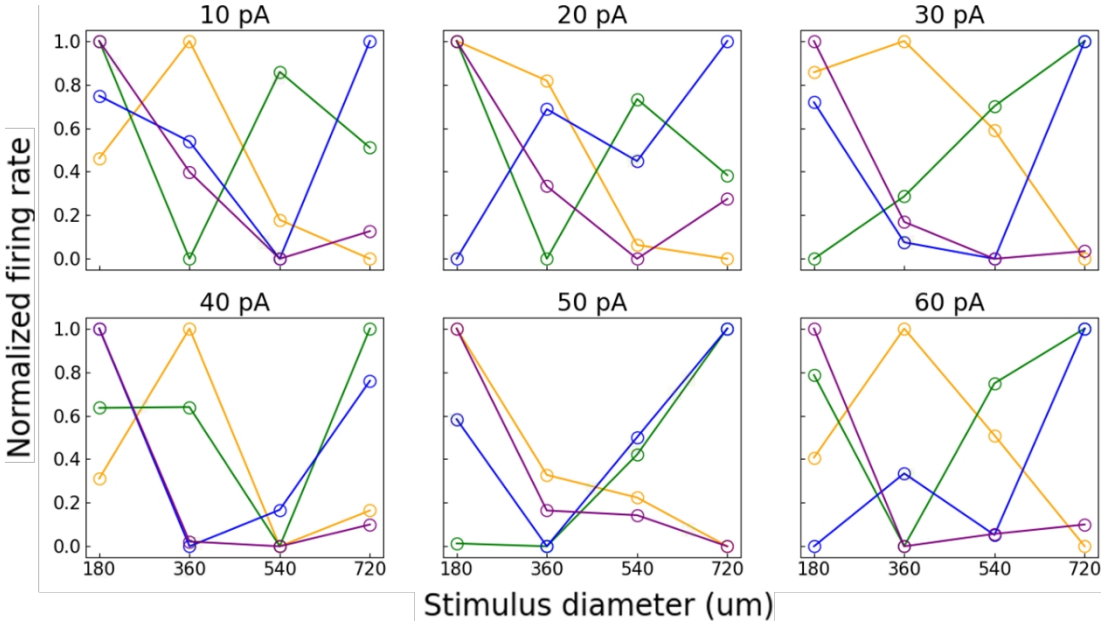

Figure 17. Layer 5 response during simulation of peri-receptive field suppression

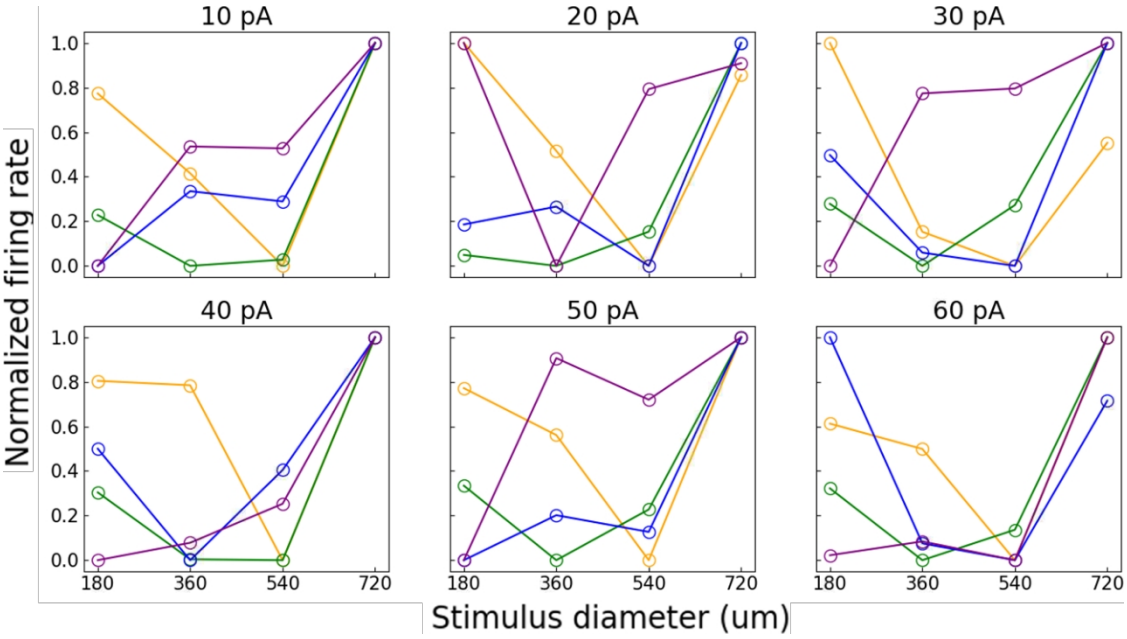

Figure 18. Layer 6 response during simulation of peri-receptive field inhibition

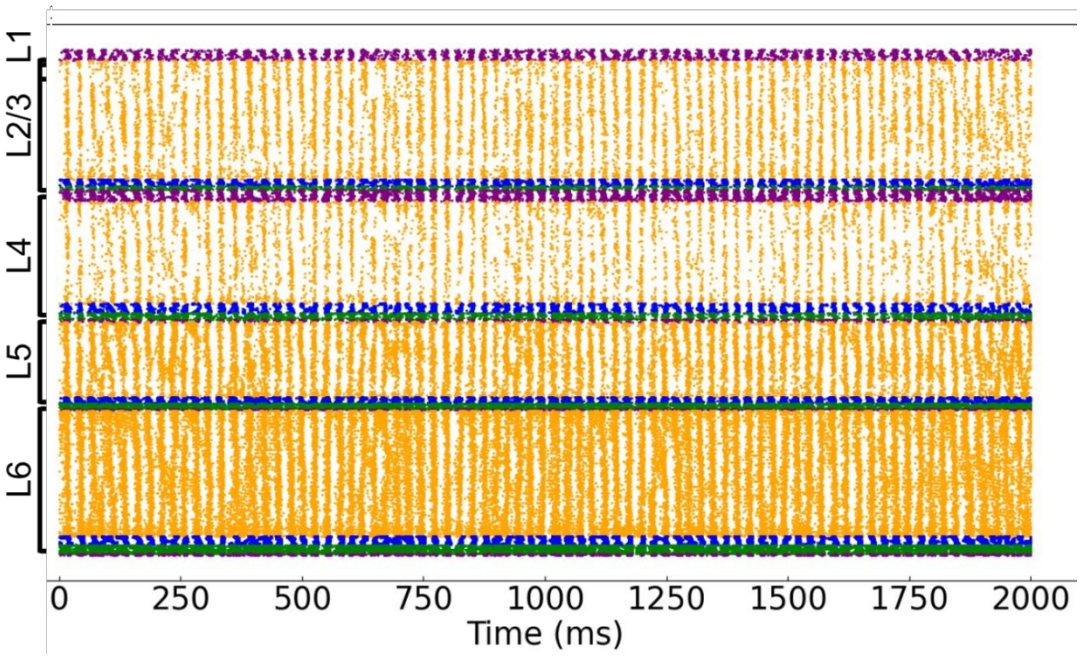

Figure 19. Raster plot of peri-receptive field suppression onset

Synchronous oscillations during peri-receptive field suppression (40 pA, 540 um) were also analyzed. As in the development of the model, we examined the frequency analysis of the total spike number change and synchronous oscillation for each 5 ms raster plot, and obtained the results shown in Figures 19-21. The frequency analysis of the synchronous vibration in Figure 21 shows that the strong peak of the γ vibration remains unchanged during peri-receptive field suppression, but the peak intensity of the γ vibration is reduced. In addition, the peak of the γ vibration became slightly broadened. In addition, there was a slight broadening of the γ vibration peak.

Overall, the results are interesting in that the average firing rate of each neuron type under peri-receptive field inhibition is greatly modulated from the unstimulated state, yet the synchronized oscillation state remains unchanged.

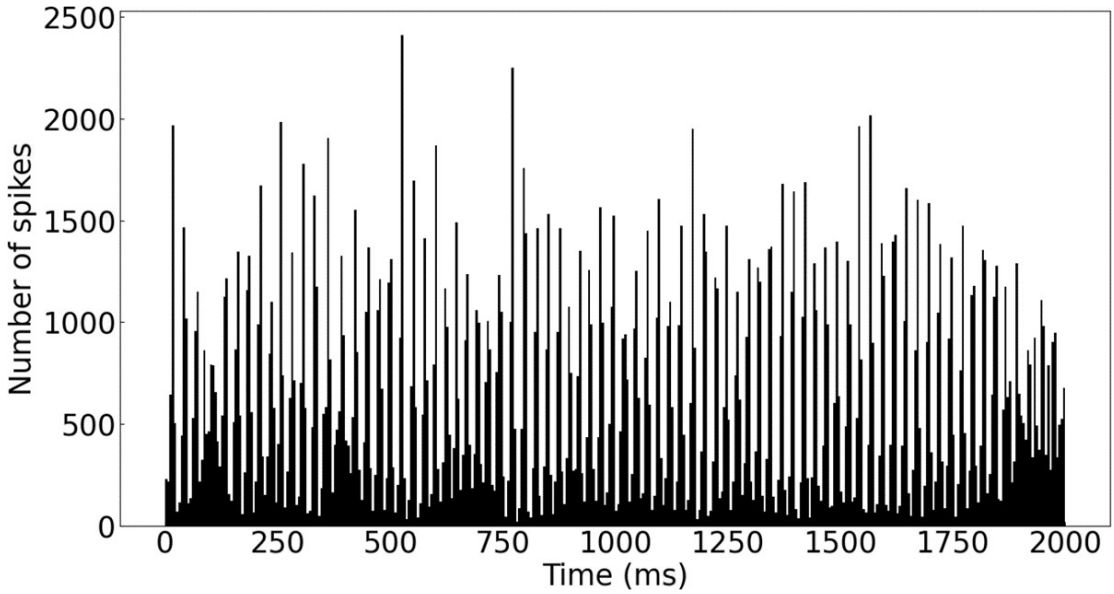

Figure 20: Change in total number of spikes per 5 ms during peri-receptive field suppression

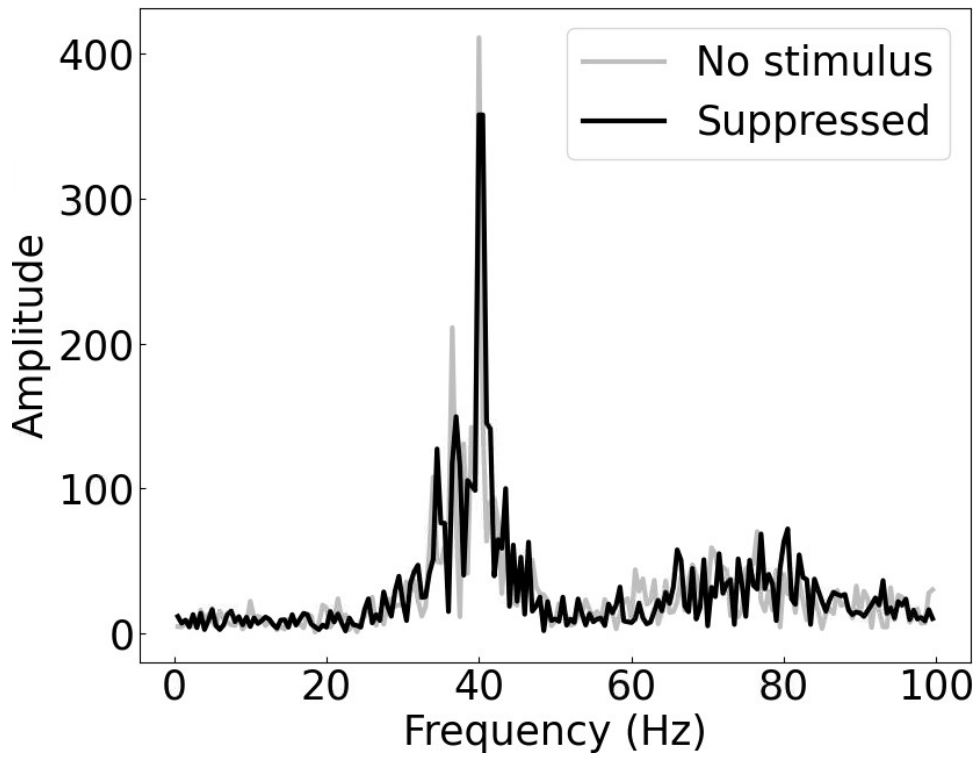

Figure 21. Frequency spectrum during peri-receptive field suppression

5.3 Comparative analysis under unstimulated and peri-receptive field suppression onset

In previous analyses, no significant differences were found in the activity of the entire column under unstimulated conditions and during the occurrence of peri-receptive field suppression. In this section, we compare the activity of the primary visual cortex model under unstimulated and peri-receptive inhibition (40 pA, 540 um condition) in more detail by using two-dimensional visualization and topological data analysis techniques.

First, the frequency analysis we have done so far is expanded to analyze temporal frequency changes by means of a spectrogram. A spectrogram is a method to visualize the temporal change of frequency as an image in which the horizontal axis represents time, the vertical axis represents frequency, and the color represents intensity, by conducting frequency analysis while sliding a time window. Figure 22 shows a spectrogram created by the Fourier transform using a time window. Here, as the signal intensity, we used the intensity in decibels calculated as $\log_{10} A$ when the transformed value is A. The left side of the figure shows the spectrogram under non-stimulation and the right side shows the spectrogram under peri-receptive field suppression, and although the visually different parts can be seen, they are not clear. Therefore, Figure 23 shows the intensity output for the ratio $\log_{10} A_2 / A_1$ when the Fourier transformed value under unstimulation is A_1 and that under peri-receptive field suppression is A_2 . The way to look at Figure 23 is to use the non-stimulus condition as a reference, with the red color indicating strong synchronous oscillations under peri-receptive field inhibition in that frequency band, and the blue color indicating weak synchronous oscillations. By looking at the figure,it can be confirmed that the peaks under peri-receptive field inhibition are stronger at various frequencies up to 1 second. After that, however, the peaks around 40 Hz and 80 Hz gradually become stronger, indicating that the non-stimulated condition has stronger peaks in a wider range. Thus, in the present simulation, it is clear that the peaks in the specific frequency range as described above become particularly strong under peri-receptive field suppression.

These results are in line with related studies [39], such as that γ -vibration improves information processing functions related to perception

If we consider the above, we can present the possibility that peri-receptive field inhibition improves perceptual information processing function, as γ oscillations are relatively stronger than in the unstimulated state. It is also consistent with the fact that peri-receptive field inhibition is a function that has advantages in the efferent coding hypothesis [21].

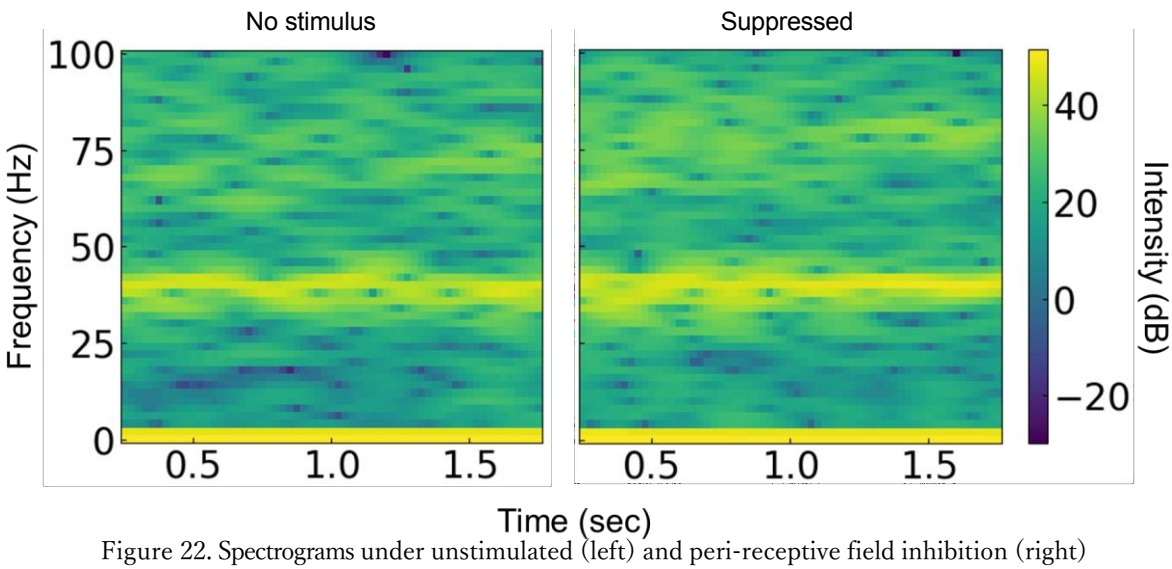

Figure 22. Spectrograms under unstimulated (left) and peri-receptive field inhibition (right)

The average firing rate (FR) and its rate of change for the entire column are then visualized in two dimensions to compare the trajectories on the plane. The average firing rate was obtained by using the change in the number of spikes every 5 ms seen so far and the total number of cells in the column. Figure 24 shows the trajectories of the average firing rate on the horizontal axis and the rate of change per unit time on the vertical axis, with the left side showing the trajectories under unstimulated conditions and the right side under inhibited conditions. As can be seen, both trajectories form elliptical trajectories inclined in the plane. Both orbits are similar and could be modeled as nonlinear oscillators like the van der pol oscillator [43]. One difference is that under unstimulated conditions, the orbit with the longest diameter takes place around 1500 ms, whereas under suppressed conditions, the orbit takes place around 800 ms. Furthermore, under suppression, the trajectory changes to take a smaller diameter trajectory at a time close to 2000 ms. For visibility, only the points on the orbit are enlarged and displayed in Figure 25.

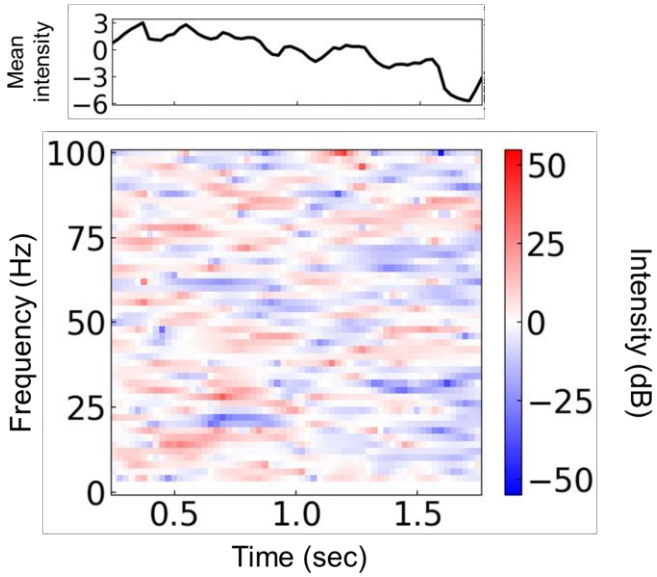

Figure 23. Spectrogram under peri-receptive field inhibition with reference to unstimulated

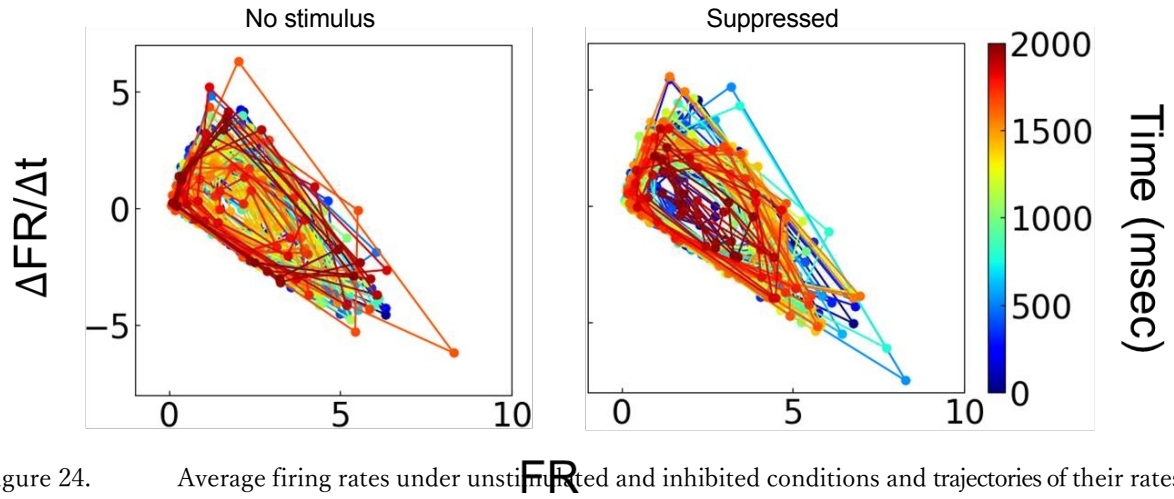

Figure 24. Average firing rates under unstimulated and inhibited conditions and trajectories of their rates of change

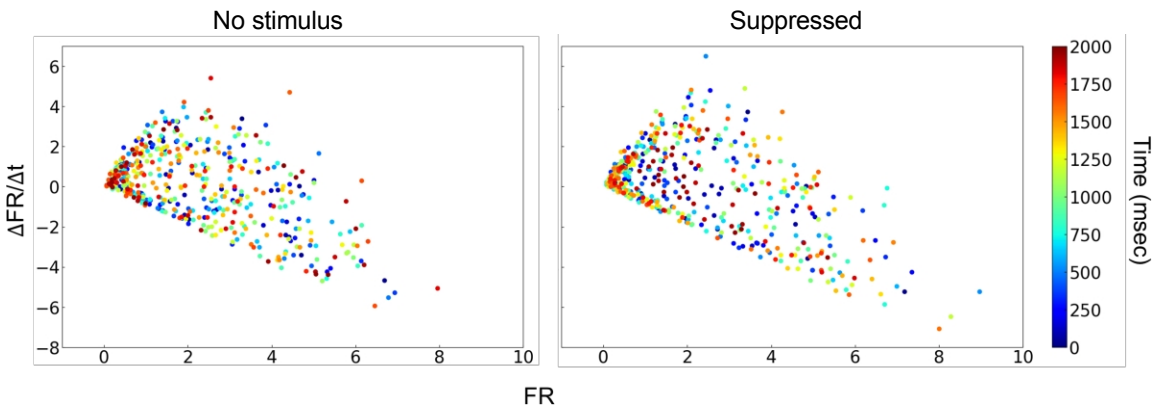

Figure 25. Average firing rates under unstimulated and inhibited conditions and points on the trajectory of the rate of change

Next, the average firing rate change described above is analyzed in a different way. The analysis method is simple: when focusing on a certain time, the average firing rate of the time of interest is taken on the horizontal axis and the average firing rate of the time following the time of interest is taken on the vertical axis, and dots are dotted across the entire average firing rate data. The output figure of this analysis is shown in Figure 26. Since dotting a single figure for all times would reduce the visibility of the point cloud structure, a figure was created for each 500 ms here. The upper part of the figure shows under unstimulated and the lower part under peri-receptive field inhibition. One of the geometric features common to both groups is that the relationship between firing rates is contained within a triangle with the origin at the apex. After 500 ms, the triangle gradually expands in the unstimulated condition, while it gradually narrows in the condition under peri-receptive field inhibition, indicating the difference between the two conditions. Furthermore, it can be confirmed that the points under peri-receptive inhibition are located on the boundary of the triangle, which is particularly prominent in the 500-1000 ms and 1000-1500 ms periods. These analyses suggest that the two states may also be distinguished by these geometric features.

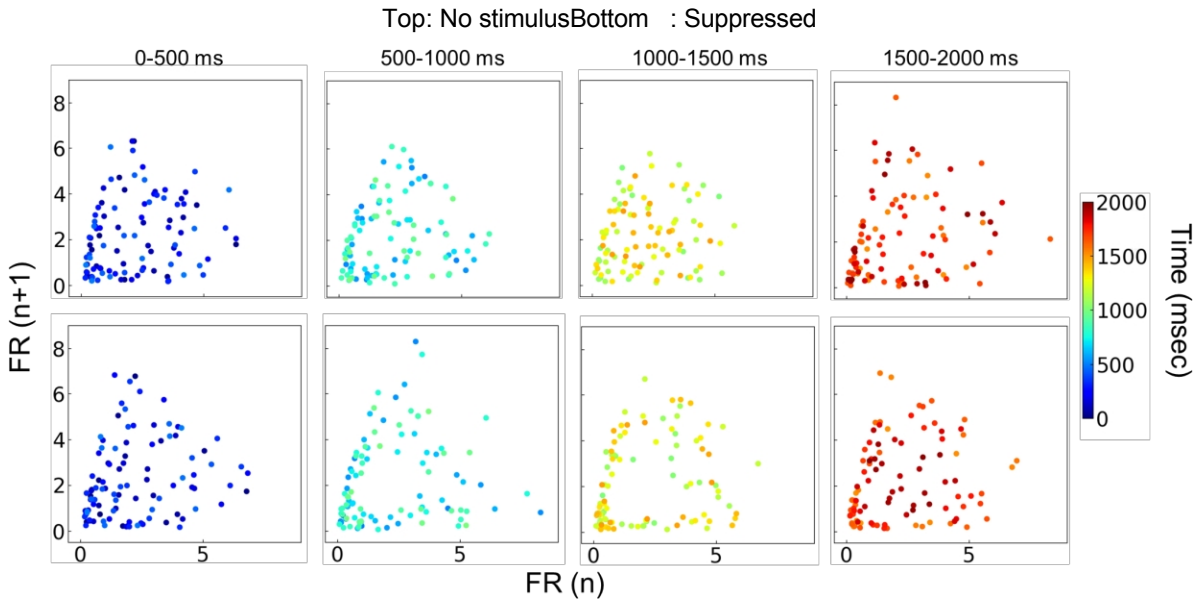

Figure 26. Relationship between time of focus and average firing rate at adjacent times.

The analysis of Figure 26 suggests that some geometric features may be relevant. Therefore, we will address the quantitative analysis of geometric features. The target is the result that a group of points under the peri-receptive field suppression is located on the boundary of the triangle, which is noticeable at 1000-1500 ms. Abstractly speaking, we can say that there is a hole in the boundary because there are almost no points inside the boundary. Therefore, topological data analysis is a powerful tool to quantitatively investigate whether or not there is a hole and what kind of hole it is. The method we will use is called persistent homology [44,45]. This is a method that gradually increases the diameter of a point cloud and examines when holes are created and when they disappear. This provides quantitative information about the holes that are characteristic of the point cloud. For all times in Figure 26

Figure 27 is the result of applying the persistent homology technique to a summary of the point cloud in Figure 27, and such a diagram is called a persistent diagram. The left side of the figure corresponds to the unstimulated and the receptive field peri-inhibited areas. The horizontal axis shows the diameter of the connecting points that can be regarded as holes, the vertical axis shows the diameter of the collapsed holes, and the color indicates the frequency of the collapses. In other words, the higher the hole is located above the diagonal, the longer the time between the creation of the hole and its disappearance, and thus the more characteristic the hole (structure) is. Conversely, holes closer to the diagonal are those that disappeared soon after their occurrence, and thus cannot be considered very characteristic. The present results show that the basic structures of both are similar, but the most characteristic hole structures are more common under the peri-receptive field suppression. Here, we examined the most characteristic structure of both as the one with the largest difference between onset time and disappearance time, and found that it corresponds to a point located near the coordinate value of (0.069, 0.27). Figure 28 shows a back-analysis and display of which part of the original point cloud this structure corresponds to. Figure 28,

Output of point clouds near the boundary of the triangle under the peri-receptive field suppression identified in Figure 26 as characteristic

The unstimulated cells are small hole structures, whereas the stimulated cells are small hole structures. This confirms the existence of such structures in a quantitative manner. Although it is not clear why such structures and point clusters exist, we believe that we have demonstrated the possibility of finding geometric features in the behavior of peri-receptive field inhibition.

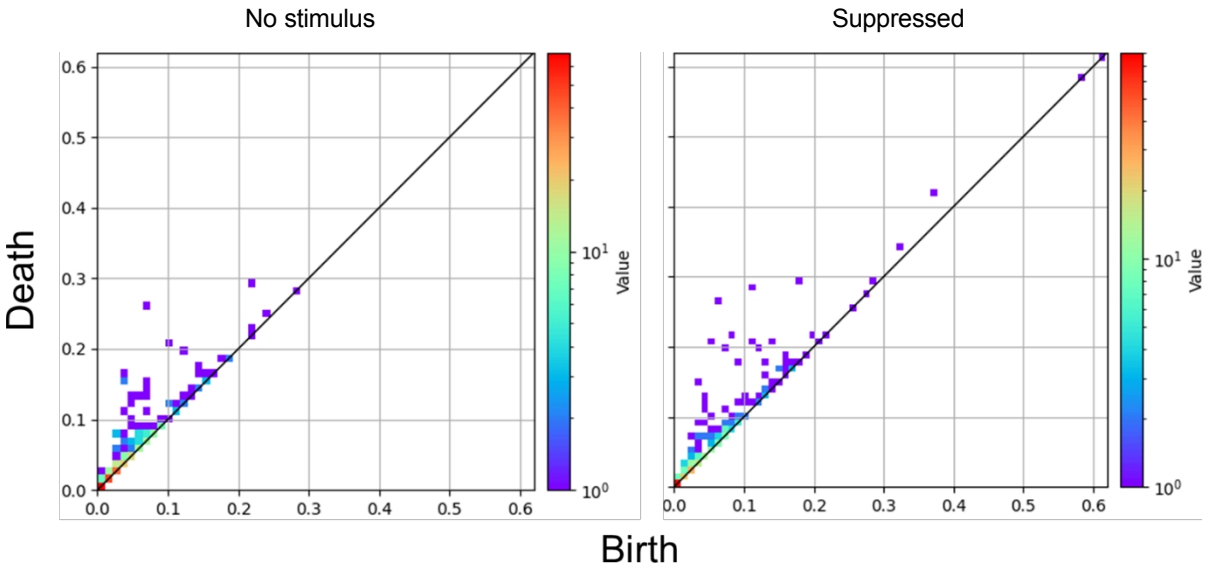

Figure 27. Persistent diagram based on the point cloud in Figure 26 under unstimulated (left) and peri-receptive field inhibition (right)

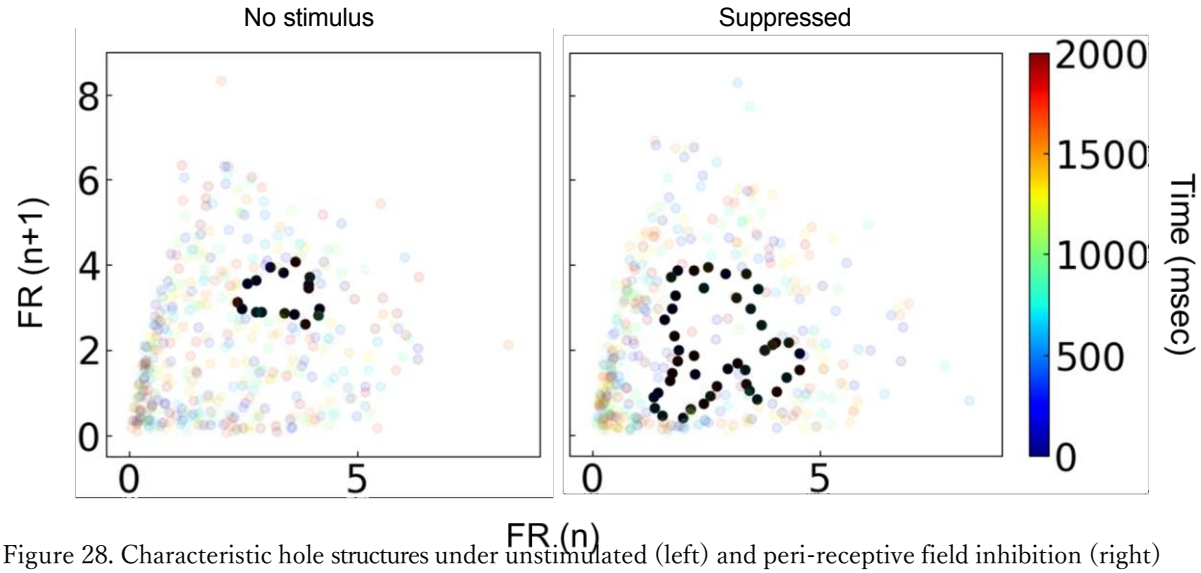

Figure 28. Characteristic hole structures under unstimulated (left) and peri-receptive field inhibition (right) obtained from persistent diagram

6 Conclusion.

In this study, we developed a new mouse model of the primary visual cortex in the waking state and reproduced peri-receptor inhibition for the first time in a model faithful to the cell density of the actual mouse brain by simulating it on the developed model. In the development of the model of the primary visual cortex in the waking state, we used a model with one to six layers of cusps based on the number of cells faithful to physiological experiments. A network with a Ram structure was constructed and adjusted to a state close to the average firing rate of the waking state by the background stimulus. The adjusted network was simulated for 2000 ms, and raster plots showing the timing of firing for each cell were generated. To determine the frequency of the synchronous oscillation, the firing rate of the entire network was determined every 5 ms, and Fourier analysis revealed a peak of γ oscillation at 35-40 Hz.

In the simulation of peri-receptive field suppression, current stimuli of various intensities corresponding to the stimulus range of physiological experiments were applied to the resting state primary visual cortex model we developed in layer 2/3. The simulation results were most consistent with the results of the physiological experiments when electrical stimulation of 40 pA was applied to layer 2/3. However, as the current intensity increased away from 40 pA, the response became different. There was also a departure from experimental values when the stimulus diameter was closer to the model's range. This is thought to be due to the fact that as one approaches the range of the model, one is more likely to deviate from the boundary conditions to reality. This suggests that responses may also change when stimulus intensity is different. The simulation results showed that the suppression index, a measure of the degree of peri-receptive inhibition, showed a similar trend to the results of the physiological experiments. The simulations also showed that Htr3A, which was not observed in the physiological experiments, responded similarly to PVs when peri-receptive field suppression was reproduced.

In addition, we simultaneously examined the response in the deeper layers, which had not been investigated experimentally: when the 2/3 layer was stimulated at 40 pA
The results showed that Pyr also produced peri-receptive field inhibition in the deeper layers in the 2/3 layer. However, the response of inhibitory cells was different from layer 2/3. This suggests that although peri-receptive field inhibition occurs in all layers, the role of inhibitory cells may differ from layer to layer. At the same time, FFT frequency analysis of the whole column activity under peri-receptive field inhibition did not reveal any significant difference from that under non-stimulation.

In order to clarify the difference between the behavior under unstimulated and peri-receptive field suppression, we analyzed the temporal variation of frequency by spectrogram, visualized the temporal relationship of average firing rate on a two-dimensional plane, and analyzed topological data using persistent homology. The spectrograms revealed that the peaks around 40 Hz and 80 Hz in the columns under peri-receptive field inhibition became larger with time than in the unstimulated condition. In addition, the method of examining the temporal relationship of the average firing rate on a two-dimensional plane pointed out the existence of nonlinear oscillatory trajectories and characteristic geometric structures. By using topological data analysis to confirm the existence of the characteristic geometrical structures, we were able to quantitatively demonstrate the existence of such structures. Although the reason why such structures are generated is unknown, we have presented the possibility that the geometric features can be used to examine the behavior of the phenomenon of peri-receptive field inhibition.

From the above, it is clear that the role of inhibitory cells in peri-receptive field inhibition changes depending on the intensity and layer of the stimulus

The results of the study were This is something that cannot be interpreted by the qualitative explanations given in previous studies. Furthermore, by analyzing the behavior of the peri-receptive field suppression phenomenon in an appropriate manner, we were able to capture its geometric features. This approach may lead to the discovery of more detailed physics in peri-receptive field inhibition. In the future, we would like to elucidate the function of peri-receptive field inhibition in more detail by expanding the size of the network and simulating different stimulation methods.

7 thanks

This research was carried out under the enthusiastic guidance of Professor Micheletto Ruggiero. I would not be where I am today without Professor Micheletto's kind and free spirit, which allowed and supported me to try various research challenges even as an undergraduate student. Although I am sure I have caused him a lot of trouble, I am happy to have been a member of Professor Micheletto's laboratory. Thank you very much for all the help and support you have given me. Thank you very much.

My secondary advisors, Professor Masashi Tachikawa, Associate Professor Shinji Nonose, and Professor Kazuo Yoshimoto, gave me advice on student life and research at the secondary advisor meeting and the interim master's presentation, and supported me in my daily life and research. Thank you very much.

I would also like to thank Assistant Professor Sun Zhe of Juntendo University for giving me the opportunity to work on neural circuit simulation. He guided me through the fundamentals and helped me reach this kind of master's thesis. Thank you very much.

D. student in our laboratory, Mr. Torataro Oikawa, always helped me with discussions at laboratory meetings and conference presentations, which was very encouraging to me. He also took the lead in various activities of the laboratory. After his arrival, the laboratory became more active and it was the most fulfilling period for me. I would like to thank you again. Yuya Shirakawa, who was my classmate in the lab, was a strong support for me when we talked, as we had many common events such as going to RIKEN together and job hunting. Thank you very much. Taiyo Kono, a junior, and I worked on research together and I myself learned a lot from him. Thanks to Kohno-kun, I was able to enjoy my daily research activities. Thank you very much. Other lab members also helped me a lot through many discussions and chats during daily research activities.

Finally, I would like to express my gratitude to my family for their constant support.

8 Research Publications

Computational Neuroscience

Paper Presentations

1. Salustri Marcello, Yoshida Shunra and Micheletto Ruggero, Neural and axonal heterogenety improves information transmission, Physica A: Statistical Mechanics and its Applications.

In addition to the above, this master's thesis research will be submitted to an international journal

Conference Presentations

1. Shun-Liang Yoshida, Z. Sun, and Michelette Ruggiero, Surround suppression in a mouse model of primary visual cortex, The 33rd Annual Meeting of the Neural Circuit Society of Japan (2023).

Semiconductor properties field

Paper Presentations

1. Shunra Yoshida, Yusuke Fujii, Giovanni Alfieri and Ruggero Micheletto, The influence of water and ethanol adsorption on the optical blinking in InGaN quantum wells, Semiconductor Science and Technology.
2. Shunra Yoshida, Yusuke Fujii, Giovanni Alfieri and Ruggero Micheletto, Time-correlated Luminescence Blinking in InGaN Single Quantum Wells, Applied Physics Letters.

In addition to the above, a study applying a delayed random walk model to the theory of blinking phenomena in InGaN single quantum wells will be submitted to an international journal

Conference Presentations

1. Shunra Yoshida, The influence of water and ethanol adsorption on the optical blinking in InGaN quantum wells, Joint IAMS-NTNU-YCU Online Workshop 2022. (2022)
2. Shunra Yoshida, Yusuke Fujii, Giovanni Alfieri and Ruggero Micheletto, A Theoretical Model of Optical Blinking Based on Temporal Correlation in InGaN Quantum Wells, Conference on Applied Geochemistry.
3. Shunra Yoshida, Giovanni Alfieri and Ruggero Micheletto, Time-correlated Luminescence Blinking in InGaN Single Quantum Wells, 14th International Conference on Nitride Semiconductors.

Image Processing Engineering

Conference Presentations

1. Shunryo Yoshida, Tetsu Sun, Makoto Yoshizawa, Takashi Michikawa, Shigeho Noda, Ruggero Micheletto, Hideo Yokota, Dynamics at Low Bandwidth

A Study on Compression and Restoration by Sampling Based on Visual Characteristics for Image Communication, The Vision Society of Japan

Summer Meeting (2022)

2. Zhe Sun, Shunra Yoshida, Shin Yoshizawa, Takashi Michikawa, Shigeho Noda, Ruggero Micheletto and Hideo Yokota, Visual Importance Map Guided Image Compression for Telepresence Robotics System, RIKEN Symposium on Advanced Photon Research (2022)

Psychophysics

Paper Presentations

Plans to submit the following conference presentations to international academic journals

Conference Presentations

1. Taiyo Kono, Shunryo Yoshida, and Ruggero Micheletto, Visibility measurement in the motion-induced vanishing illusion, J. Opt.

Summer Meeting of the Vision Society of Japan (2023)

9 References

[1] Mark F. Baer, Neuroscience: Explorations of the Brain, Revised Edition, Nishimura Shoten, 2021

[2] Jane B. Reese, Campbell Biology, 11th edition, Maruzen Publishing, 2018

[3] Hirokazu Takahashi, Introduction to Brain Science for Mechanics, Nikkan Kogyo Shimbun, 2016

[4] Hirokazu Takahashi, Continued Introduction to Brain Science for Mechanics, Nikkan Kogyo Shimbun, 2017

[5] Peter Dayan, Theoretical Neuroscience: Computational and Mathematical Modeling of Neural Systems, MIT Press, 2005

[6] Eugene M. Izhikevich, Dynamical Systems in Neuroscience: The Geometry of Excitability and Bursting, MIT Press, 2010

[7] Tadashi Yamazaki, First Neural Circuit Simulation, Morikita Publishing, 2021

[8] Hodgkin, A. L., & Huxley A. F. (1952). A quantitative description of membrane current and its application to conduction and excitation in the nerve.

[9] FitzHugh, R. (1955). Mathematical models of threshold phenomena in the nerve membrane.

[10] Nagumo, J., et al. (1962). An active pulse transmission line simulating nerve axon.

[11] Lapicque, L. (1907). Recherches quantitatives sur l'excitation électrique des nerfs traitée comme une polarization. Journal de physiologie et de pathologie générale, 9, 9, 620-635. 620-635.

[12] Izhikevich, M. E. (2003). Simple model of spiking neurons. in IEEE Transactions on Neural Networks, 14, 6, 1569-1572.

[13] Hubel, D. H., & Wiesel, T. N. (1962). Receptive fields, binocular interaction and functional architecture in the cat's visual cortex.

[14] Tanaka, S. (1988). Theory of self-organization of cortical Maps. In Proceedings of the 1st International Conference on Neural Information Processing Systems, 451 -458.

[15] Swindale N. V. (1996). The development of topography in the visual cortex: a review of models.

[16] Markram, H., et al. (2015). Reconstruction and Simulation of Neocortical Microcircuitry. cell, 163(2):456-92.

[17] Billeh, Y.N., et al. (2020). Systematic Integration of Structural and Functional Data into Multi- scale Models of Mouse Primary Visual Cortex. neuron, 106, 1-16.

[18] Angelucci, A., et al. (2017). Circuits and Mechanisms for Surround Modulation in the Visual Cortex. annual Review of Neuroscience, 40:425-451.

[19] John, A. P. (2012). A neural-based code for computing image velocity from small sets of middle temporal (MT/V5) neuron inputs. Journal of Vision, 12(8):1.

[20] Kapadia, M. K., et al. (1995). Improvement in visual sensitivity by changes in local context: parallel studies in human observers and in V1 of alert monkeys.

[21] Barlow, H. B. (1961). Possible principles underlying the transformation of sensory messages. sensory communication, 217-234.

[22] Vinje, W. E., & Gallant, J. L. (2002). Natural stimulation of the nonclassical receptive field increases information transmission efficiency in V1. The Journal of Neuroscience, 22 (7): 2904- 15. 2904- 15.

[23] Solomon, S. G., et al. (2006). Suppressive surrounds and contrast gain in magnocellular- pathway retinal ganglion cells of macaque. Journal of Neuroscience, 26: 8715-. 26.

[24] Alitto, H. J., & Usrey, W. M. (2008). Origin and dynamics of extraclassical suppression in the lateral geniculate nucleus of the macaque monkey.

[25] Angelucci, A., et al. (2002). Circuits for local and global signal integration in the primary visual cortex. journal of Neuroscience, 22: 8633-46.

[26] Zhang, S., et al. (2014). Long-range and local circuits for top-down modulation of visual cortex processing. Science, 345: 660-65

[27] Carandini, M., & Heeger, D. J. (2012). Normalization as a canonical neural computation. Nature Reviews Neuroscience, 13(1):51.

[28] Ahmadian, Y., et al. (2013). Analysis of the stabilized supralinear network. neural computation, 25(8):1994-2037.

[29] Rubin, D.B., et al. (2015). The stabilized supralinear network: a unifying circuit motif underlying multi-input integration in sensory cortex. Neuron, 85(2):402- 417.

[30] Li, Y., & Young, L-S. (2021). Unraveling the mechanisms of surround suppression in early visual processing. PLoS Computational Biology, 17(4): e1008916.

[31] Adesnik, H., et al. (2012). A Neural Circuit for Spatial Summation in Visual Cortex. nature, 490(7419), 226-231.

[32] Ter W. M., & Tiesinga P. H. E. (2021). Comprehensive characterization of oscillatory signatures in a model circuit with PV- and SOM-expressing interneurons. Biological Cybernetics, 115(Biological Cybernetics, 115(5):487-517.

[33] Georgiou, C., et al. (2022). A subpopulation of cortical VIP-expressing interneurons with highly dynamic spines. Communications Biology, 5, 352.

[34] Pfeffer, C., et al. (2013). Inhibition of inhibition in visual cortex: the logic of connections between molecularly distinct interneurons. Nature Neuroscience, 16, 1068 -1076.

[35] Gewaltig, M-O., & Diesmann, M. (2007). NEST (Neural Simulation Tool). Scholarpedia, 2(4), 1430.

[36] Petersen, C. C. H., & Crochet, S. (2013). Synaptic Computation and Sensory Processing in Neocortical Layer 2/3. Neuron, 78, 1, 28-48.

[37] Hoy, J. L., & Niell, C. M. (2015). Layer specific refinement of visual cortex function after eye opening in awake mice. journal of Neuroscience, 35(8), 3370, 83.

[38] Wang, X. J. (2010. Neurophysiological and computational principles of cortical rhythms in

cognition. Physiological Reviews, 90(3): 1195-1268.
[39] Siegle, J. H., et al. (2014). Gamma-range synchronization of fast-spiking interneurons can enhance detection of tactile stimuli. Nature Neuroscience, 17(10): 1371-1379.
[40] Cardin, J. A., et al. (2009). Driving fast-spiking cells induces gamma rhythm and controls sensory responses. nature, 459(7247): 663-667.
[41] Sohal, V.S., et al. (2009). Parvalbumin neurons and gamma rhythms enhance cortical circuit performance. nature, 459(7247): 698-702.
[42] Takanori H., et al. (2017). Cortical Parvalbumin Neurons and Cognitive Deficits in Schizophrenia. Japanese Journal of Biological Psychiatry, 28(1): 32-40.
[43] van der Pol, B. (1927). On relaxation-oscillations. the London, Edinburgh, and Dublin Philosophical Magazine and Journal of Science, 2(7), 978-992.
[44] Zomorodian, A., & Carlsson, G. (2004). Computing Persistent Homology. discrete & Computational Geometry, 33 (2): 249-274.
[45] Ippei O., et al. (2022). Persistent Homology Analysis for Materials Research and Persistent Homology Software: HomCloud.